Statistical analysis of Gamma-ray emitting radio galaxies: relation between jet power and disk luminosity

(ガンマ線を発する電波銀河の統計解析：ジェットパワーと降着円盤光度の関係性について)

学位取得年月 2024年 3月

眞武 寛人

Contents

Abstract

I systematically analyzed Swift/XRT X-ray data from gamma-ray emitting radio galaxies (RGs) to investigate the origin of their X-ray radiation and the relation between jet power and disk luminosity using the obtained result of the origin of X-ray radiation for each sample RGs. To investigate the origin of X-ray radiation, I studied the short-duration variability of spectra by using Swift/XRT data for 20 RGs. I found that gamma-ray emitting RGs with a higher gamma-ray to X-ray flux ratio show a strong harder-when-brighter behavior. In addition, gamma-ray emitting RGs with soft gamma-ray spectral index tend to have a hard X-ray spectral index and vice-versa. Based on these properties, I suggest a trend that gamma-ray emitting RGs could be classified roughly into three types of X-ray emission; jet-dominated type, disk/corona-dominated type, and intermediate type. This classification is quite consistent with the optical and radio classification of RGs. I also discuss this result in terms of the Eddington luminosity ratio.

According to these 3 types of X-ray, I estimate disk luminosity using UV flux for jet-dominant RG and X-ray flux for disk/corona-dominant RG. And also, I calculate jet powers using jet model parameters estimated by multi-wavelength SED model fitting (Ghisellini et al. (2014)) and 1.4 GHz radio luminosity(Willott et al. (1999)). As a result, for RGs, the jet power estimated by SED shows quite close distribution with Ghisellini's Blazars when the RG is considered to be observed disk/corona in X-ray. Thus, jet power shows higher disk luminosity and 10 times higher the energy of accretion matter. This power is considered to be produced by the extraction of the rotational BH energy through the magnetic field by the BZ mechanism. In addition, I also calculate jet power by radio luminosity for 3 types of AGN, but they do not show the same relation between jet power and disk luminosity. I consider this to be due to the beaming effect (inclination angle), which needs to be taken into account in the jet power calculations.

1 Introduction

1.1 Active Galactic Nuclei

It is widely known that supermassive black holes (SMBH) exist at the center of almost all galaxies and have masses of 10^6 – 10^9. The central region of galaxies bright in the broad wavelength band when accretion flow is formed around them. The objects with these features are called an active galactic nucleus (AGN). There are several subclasses of AGNs. The two main types of AGNs are radio-loud (RL) AGN and radio-quiet (RQ) AGN. The RL-AGN exist about 15% - 20% of AGNs (Urry & Padovani, 1995), which exhibits a relativistic jet. If the jet is observed out of the line of sight, The RL-AGN are classified as radio galaxy (RG) or misaligned AGN (MAGN). And also, small fraction of RL-AGNs is classified as Blazar if the viewing angle of the jet is within a few degrees. On the other hand, the majority of AGN is classified as RQ-AGN, and Seyfert galaxy and RQ-Quasar are classified as this class. There is another mainly classification that is using permitted line width: the object with around 1,000 km/s of half width of permitted line is classified as type I AGN, and the object with around few hundred km/s of half width of permitted line is classified as type II AGN. Nowadays the AGN unified theory that all AGN classifications are created because of difference of inclination angle become mainstream Ref. (2). Based on this theory, I can illustrate Seyfert I and II, RGs, and Blazars easily and explain their features.

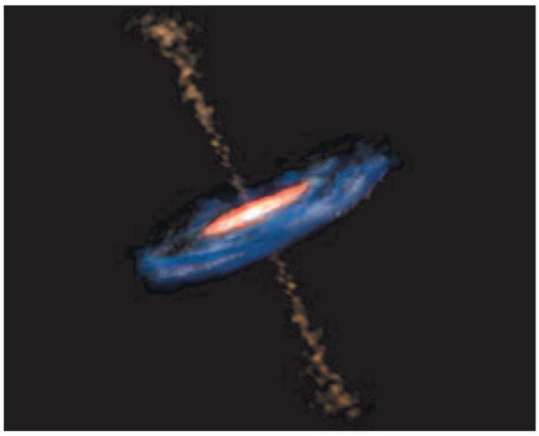

Figure 1: Image of AGN ?

1.2 Seyfert Galaxy

Seyfert galaxy is one of the RQ-AGN class, and it is known that the jet radiation from center part is very week or nothing. There are lots of spectral lines in optical wavelength, and they are classified as type I or type II by the verbosity width calculated using line width. Seyfert I objects have wide around few 1,000 km/s verbosity width, and Seyfert II objects have around 500 km/s verbosity width. This difference in velocity is related to the distance between the emitting region and the BH. It is thought that emission lines with large velocity widths appear in the spectrum from the wide emission line region (BLR) close to the BH, while emission lines with low velocity widths appear in the spectrum from the narrow emission line region (NLR) far from the BH. The gas density (electron density) is also different in these different emission regions. As a result, different types of emission lines are observed: forbidden lines from NRL and allowed lines from BLR. Furthermore, the accretion disk is formed around the BH, which is surrounded by the optically thick molecular cloud torus, and radiation is greatly absorbed through the torus. Therefore, based on the AGN unified theory (see Figure1), Seyfert type I can observe radiation from the BLR and NLR relatively close to the BH, while in Seyfert type II, radiation from the BLR is absorbed by the torus and only radiation from the NLR can be observed. X-ray emissions from AGNs are largely considered to be

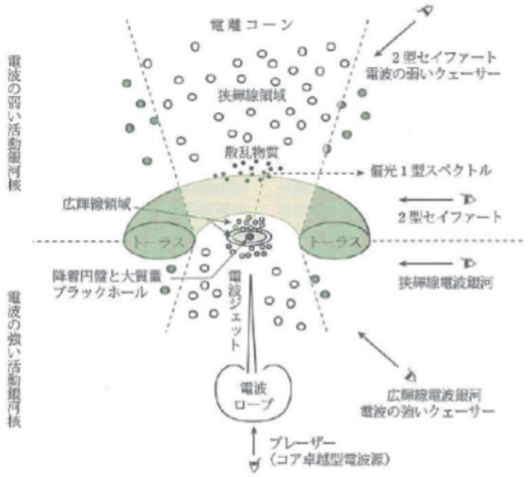

Figure 2: AGN unified theory Ref. (2)

jet-derived and accretion disk-derived, but since X-ray emissions from Seyfert galaxies are weak in jet emissions, X-ray emissions are considered to be emitted from the accretion disk and corona.

In the accretion disk that is formed around the BH, the gas falls into the BH as it rotates, but because the velocity of the accretion gas varies with radius, angular momentum is carried toward the outside of the disk and the gas felt toward the center due to viscosity. The accretion disk is heated by viscous friction caused by the angular momentum transported by the viscosity, and this thermal energy is emitted outward as radiation energy. This is thermal radiation, which is observed as the disk blackbody radiation spectrum. Since the viscous friction becomes stronger as one approaches the center of the BH, the radiation near the BH is observed as higher-energy ultraviolet radiation. A part of ultraviolet radiation is converted to X-ray radiation by the inverse Compton scattering in a thin body of gas (corona) around the accretion disk, which is hotter than the accretion disk (Figure 1.3, left panel). X-ray radiation from the corona is also reflected by the accretion disk, resulting in X-ray emission as well. This mechanism of radiation from the accretion disk is considered as radiation from the standard accretion disk, and Figure 1.4 shows the radiation spectrum from the standard accretion disk.

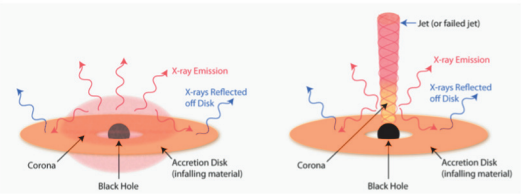

Figure 3: Image of AGN **?**

However, when the amount of accretion material is very low or high, advection-dominated accretion disks (ADAFs) and supercritical accretion disks are formed, respectively, and the radiation model differs from that of standard accretion disks. In ADAFs, the accretion disk is optically thin due to the small amount of accretion material. The ADAF also has thermal energy due to viscous heating, but because the accretion material (gas) is dilute, radiative cooling does not work sufficiently, and the gas is heated to a higher temperature, forming a geometrically very thick disk, and this thermal energy falls into the BH instead of being radiated. Furthermore, because the gas is dilute, the radiation from this disk is not blackbody radiation, but mainly thermal bremsstrahlung,

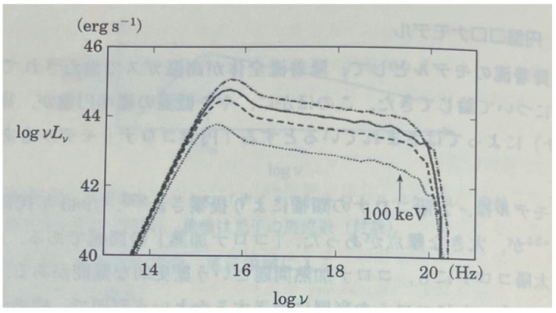

Figure 4: AGN unified theory Ref. (2)

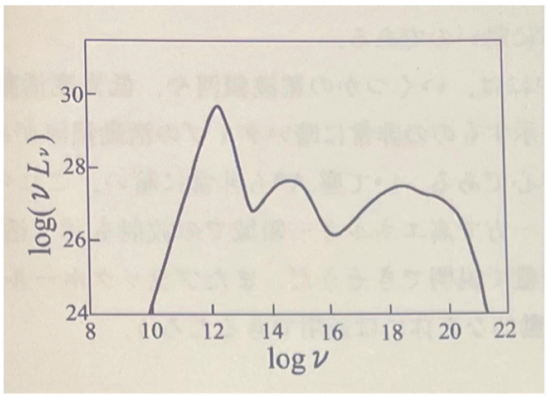

Figure 5: AGN unified theory Ref. (2)

which is caused by the orbital bending of energetic electrons around ions, synchrotron radiation, which is caused by the orbital bending of energetic electrons around magnetic fields, and inverse Compton scattering [4]. Therefore, non-thermal radiation characteristic of power-law spectra is observed from the ADAF, as shown in Figure 1.5. In Figure 1.5, three peaks are observed, from the left: infrared photons from synchrotron radiation, ultraviolet photons from backward Compton scattering of infrared photons, and X-ray photons from backward Compton scattering and thermal bremsstrahlung. I can see that the overall radiation distribution is a power-law with a steep rightward decline.

1.3 Blazar

Blazar is classified as a radio-loud AGN and is considered to be observing the radiation-emitted from the relativistic jet aligned toward the line of sight. Since the emission is observed over a wide energy range from radio waves to gamma rays, studies using multiple wavelengths have been active in recent years. Jet radiation is greatly affected by relativistic beaming effects. As a result, it becomes apparently very bright against the disk emission, since particle acceleration takes place in the jet, the emission reaches GeV and/or TeV gamma-ray energy. The multi-wavelength spectrum (SED) of the Blazar is characteristic, and when plotted on the axes of "frequency ν" and "flux multiplied by frequency parameter νF_ν", two peaks appear on the SED (Figure 6). The two peaks on the SED are considered to be due to different mechanisms, and the low-frequency peak is considered to be due to synchrotron radiation. On the other hand, several radiation models have been proposed for the high-frequency peaks. The main models are the leptonic model, the hadronic model, and the lept-hadronic model, which is a combination of the former two. They are summarized below.

- leptnic model
  The model is based on the assumption that the radiation is composed of leptons (electrons and positrons) and that only the leptons are accelerated and the hadrons are not accelerated to high energy. The electrons that produce synchrotron radiation at low frequencies also inverse-Compton-scatters synchrotron photons to X-ray or gamma-ray, which are considered to create a high-frequency peak. This is called as the Syncrotron Self-Compton (SSC) model. For high-luminosity Blazars, the External Compton (EC) model, in which infrared or optical radiation from accretion disks, BLRs, and toruses is back Comptonized by electrons in the jet, is also considered.

- hadronic model
  Both electrons and protons are accelerated to relativistic energies. The accelerated protons produce three types of pions (π^0, π^+, π^-). The high-frequency pions are considered to be composed of synchrotron radiation from protons and gamma-ray radiation from π^0 decays, synchrotron radiation and Compton scattering from the secondary decays of π^+, π^-, and gamma-ray cascades. Since neutrinos are produced during the decay of π^+, π^-, successful observation of neutrinos associated with the jet radiation would provide solid evidence to explain this model.

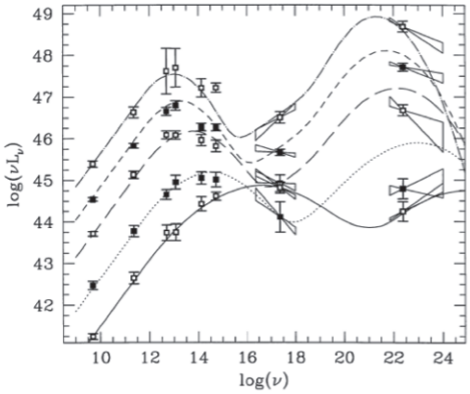

Figure 6: Blazar SED*Fossatietal.* (1998)

The lept-hadronic model is a combination of SSC by lepton and proton synchrotron radiation by hadron. However, following the recent observation of neutrinos associated with radiation from a blaser (TXS 0506+056) observed by IceCube, the hadronic and lepto-hadronic models are beginning to be accepted. Blazars can also be classified into two types, BL Lac and FSRQ, based on visible light spectral observations; BL lac is considered to be the less luminous source and FSRQ is the more luminous source. In Figure refblazar, the dashed spectra with synchrotron radiation peaks at lower frequencies represent FSRQs, while the solid spectra on the higher energy side represent BL lacs.

1.4 Radio Galaxy

RGs are classified as RL-AGNs like Blazars, and are objects whose jet emission has been observed in radio images along with emission from the central core. The major difference from Blaser is that radio galaxies are miss-aligned AGNs (MAGNs) that observe the jet at an angle off the line of sight. Thus, radio galaxies are less affected by the beaming effect of the jet emission, and the emission from their cores is weaker than that of Blazars. Therefore, the observed radiation includes radiation from the accretion disk and the corona near the center of the BH, in addition to the jet core. Because of the presence of radiation from sources other than jets, radio galaxies are considered to be important for understanding the relationship between the jet and the accretion disk, as well as the structure of jets. While it is believed that radiation from accretion disks and coronas has been observed, it is also characterized by fewer number of detections in gamma rays compared to Blazar due to the weak beaming effect.

RGs are mainly classified in the radio and optical bands. Classification in the radio band is based on the Fanaroff-Riley (FR) classification (Fanaroff & Riley (1974)): RGs are classified as FR-I if the radio luminosity at 178 MHz is less than 10^{26}[WHz^{-1}] and FR-II if it is greater than 10^{26}[WHz^{-1}] (Tadhunter (2016)). In their morphology, FR-Is show weak jet collimation and the brightness of the jet reduces at larger distances from the core, whereas FR-IIs show strong jet collimation and bright hot spots at the edge of the jets (Figure 7).

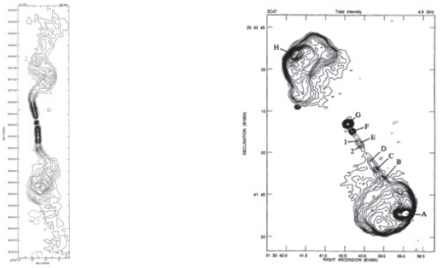

Figure 7: radio image of FR-I (left) and FR-II (right)$Fanaroff\&Riley$ (1974)

The FR classification is basically morphological, according to where most of the luminosity is radiated. This division roughly translates into a separation in radio power. However, the origin of the FR dichotomy is still unexplained. Among the possible explanations, Ghisellini & Celotti (2001) proposed the accretion rate. The other classification is based on optical emission lines. They are classified as high excitation RGs (HERG) if the [OIII]5007/Hα line ratio is greater than 0.2 and the equivalent width of [OIII] is greater than 3 Å, whereas they are classified as low excitation RGs (LERG) if the [OIII] line is relatively weak (Laing et al., 1994). In addition, HERG and LERG have been classified based on the Excitation Index (EI) (Buttiglione et al. (2010)). This parameter, EI, is a spectroscopic indicator that measures the relative intensity of low and high excitation lines, making it more stable than single-line ratios. In this study, I call the objects FR-I/LERG if they are classified as FR-I and LERG. The less powerful RG has inefficient and hot accretion flow like ADAF, and the powerful RG has efficient accretion with cold gas like a standard disk (Heckman & Best (2014)). Therefore, FR-Is could have a low accretion rate, and FR-IIs could have a high accretion rate. HERG/LERG classification is also related to the accretion mode, but combinations of classifications are complex. Macconi et al. (2020) used 79 3CR objects with z < 0.3 and show 30 FR-II/HERG and 17 FR-II/BLRG, 19 FR-II/LERG, and 13 FR-I/LERG. On the other hand, according to FRICat and FRIICat by Capetti et al. (2017)a, b where sample RGs are at z < 0.15, all FR-I objects show the Low Excitation galaxy, and 90 % of FR-II objects show the Low Excitation galaxy and 10 % of FR-II objects show the high excitation galaxy. The FR classification and the optical classification are also related to a quantity of cold gas obscuring X-ray and dust in a galaxy affecting optical measurements, respectively (Macconi et al. (2020)). Several studies also interpret FR-II/LERG as FR-II/HERG aged and depleted of cold gas or as an intermediate classification between FR-I/LERG and FR-II/HERG (Gendre et al. (2013), Macconi et al. (2020), Grandi et al. (2021)). However, these interpretations are still under discussion.

1.5 The aim of this study

Based on 10 years of observations using Fermi/LAT, the 4FGL-DR2 catalog (4th Fermi-LAT Gamma-ray Source Catalog Data Release 2) was released in 2020 (Ballet et al., 2020), which showed that the number of RGs detected in the GeV gamma-ray band has increased considerably. The spectral energy distribution (SED) of bright RGs is well represented by the one-zone synchrotron self-Compton (SSC) model (Fukazawa et al., 2015), which explains two peaks on the SED; the low energy peak corresponds to the synchrotron radiation and the high energy peak corresponds to the SSC radiation. This model is known to represent the BL Lac Blazar SEDs correctly (e.g. Kubo et al. (1998)). However, several studies reported that the one-zone SSC model is not sufficient for some RGs and BL Lac objects (Boccardi et al. (2019), Abdo et al. (2009), Fraija et al. (2017)). Nevertheless, an understanding of the X-ray emission from RGs is not established. Emissions from both disk/corona and jets are observed in the X-ray band (e.g. Kataoka et al. (2007), Fukazawa et al. (2018)); hence, it is required to understand the X-ray emission

of RGs to evaluate their SEDs (Yamazaki et al., 2013). In a previous systematic study on the X-ray radiation of RGs (Fukazawa et al., 2015), not only the X-ray spectral index but also X-ray variability, Fe-Kα line, and [OIII] line luminosity were investigated. They indicate that the X-ray radiation is likely to be from the jets in the case of LERGs and from the disk/corona in the case of HERGs. However, their sample contains only eight sources based on Fermi/LAT first catalog. A large number of sample RGs are required to obtain a complete picture. In this context, I used the samples from the 4FGL-DR2 catalog to increase the number of sample RGs. The radiation is unlikely to be disk/corona emission if the X-ray spectrum is steep. If the X-ray spectrum is hard, it is also difficult to determine whether it is disk/corona radiation or non-thermal jet radiation. Therefore, in this study, properties other than the X-ray spectrum are considered in discussing the X-ray origin.

Since the increase in the sample size allows us to perform statistical analysis of radio galaxies, I investigate the relationship between jet power and disk luminosity. Two main results were obtained in previous studies. In Ghisellini et al. (2014), using Blazar as a sample, jet power was estimated from SED, with the result that the jet power shows an order of magnitude larger than the disk luminosity. In contrast, Inoue et al., 2017, using Radio Loud Quasar (RL-Quasar), estimated jet power from radio luminosity, which shows that the disk luminosity is about an order of magnitude larger than the jet power. Based on the AGN unified theory, the relationship between jet power and disk luminosity should be equivalent for RL-Quasar and Blazar because all AGN sources just depend on the angle from which they are viewed and the existence of jet. Therefore, I consider that there are two factors contributing to this difference in results. One is the possibility that different viewing angles (or different types of objects) contribute to the estimation of jet power or disk luminosity, and the other is due to the different estimation methods of jet power or disk luminosity and their uncertainties. To confirm both, I use two estimation methods of jet power by radio luminosity and SED, using RGs observed in gamma-ray and the samples of the previous paper (Ghisellini et al. (2014) and Inoue et al. (2017)), and compare the results with those of the two papers. After that, I discuss why the results differ among different previous studies and consider a more appropriate relationship between jet power and disk luminosity.

I present my sample RGs and X-ray and Gamma-ray data in Section 2, data analysis in Section 3, and analysis methods in Section 4. I present my result of the X-ray analysis and the relation between jet power and disk luminosity in Section 5 and Section 6, respectively. And I conclude my study in Section 6. The cosmological parameters that I assumed are $H_0 = 70 \mathrm{kms}^{-1}\mathrm{Mpc}^{-1}$, $\Omega_M = 0.3$, and $\Omega_\lambda = 0.7$.

2 X-ray and Gamma-ray data

2.1 Fermi

The Gamma-ray Observation Satellite Fermi is a satellite that observes the energy band of gamma-rays, mainly from 20 MeV to 300 GeV, with a wide field of view to reveal high-energy phenomena in the universe. It was launched in 2008 and is still in operation. It carries two detectors, the Large Area Telescope (LAT) and the Gamma-ray Burst Monitor (GBM), with the LAT being the main detector and the GBM being a complementary detector. The main performance of the LAT and GBM is summarized in Table 1. The main performance of LAT and GBM is summarized in Table 1 below, and the observation method of LAT is described in the next section. After that, the FGL (Fermi Gamma-ray LAT) catalog using LAT observations is described.

	Large Area Telescope	Gamma-ray Burst Monitor
Detective energy	20 MeV - 300 GeV	8 keV - 40 MeV
FOV	2.4 sr	9.5 sr
Angular resolution	$<1^\circ$ (1 GeV)	3°(Gamma-ray burst)
Time resolution	1 μsec	2 μsec

Table 1: Performance of LAT and GBM

2.1.1 LAT

As mentioned in the previous section, the LAT observes the energy band from 20 MeV to 300 GeV and is particularly sensitive from 1 GeV to 100 GeV. The detector consists of four subsystems as shown in Figure 9, which detect gamma rays and remove cosmic rays and charged particles. Finally, the Data Acquisition System (DAQ) transmits and acquires the data to the ground. The four subsystems are described below.

- Tracker, Conversion foil
  Gamma rays are detected by layers of tungsten sheets and silicon strip detectors. There are 16 layers, with silicon strip detectors located above and below each tungsten sheet. The 16 layers of tungsten sheets interact with incident gamma rays and produce electron-positron pair production. The charged particles produced by the pair production are detected by the silicon strip detector, allowing precise measurement of the passing position.

- Calorimeter
  The charged particles produced by pair production eventually enter the calorimeter, which absorbs the total energy and measures the energy of the particles. It consists of a cesium iodide (CsI) scintillator.

- Anticoincidence Detector
  It removes 99.97% of the charged particle signals produced by cosmic rays and gamma rays. It also removes gamma radiation from the direction of the earth's atmosphere. It consists of plastic scintillator tiles.

- DAQ
  Data acquisition equipment, which collects information from the Anticoincidence Detector, Tracker, and Calorimeter, and transmits the information on cosmic rays and gamma rays to the ground separately.

2.1.2 FGL catalog

There are several Fermi/LAT catalogs, but they are different in terms of energy range and number of detected sources. In particular, the FGL(Fermi Gamma-ray LAT) catalogs gamma-ray emitting sources in the LAT detection energy range of 0.02 - 300 GeV. Starting with the 1FGL catalog, the number of detected sources in the catalog has increased through improvements in not only photon statistics, but also analysis methods, calibration methods, galactic radiation (diffuse) models, and event reconstruction. The 4FGL-DR2 catalog used in this study is the fourth catalog in the FGL (Fermi Gamma-ray LAT) catalog and contains objects detected using data from the 10 years (2018) since the beginning of the mission (around 2008). Compared to the third 3FGL catalog, the 4FGL catalog has all new analysis methods, calibration methods, galactic radiation (diffuse) models, and event reconstruction, and the total number of detected sources has increased significantly from 3033 to 5787. Sources in the 4FGL catalog are included based on statistical detection significance over the entire period analyzed, and do not include transient gamma-ray bursts, solar flares, or most novas. One of the features of the 4FGL catalog is that it has twice as long an exposure time as the 3FGL catalog. Other differences from the 3FGL catalog include new IRFs and galactic radiation models. IRFs (Instrument Response Functions) are, as the name suggests, response functions of detection instruments, which are used for LAT analysis based on mapping information between incident flux and detection events. The Galactic radiation model is a model that takes into account gamma-ray emissions from the interaction of interstellar gas and cosmic rays in the Galaxy, and is provided as a spatial and spectral template in the LAT analysis. And also, the model is modified by using information on HI and CO emission lines. In addition to the FGL catalog, there are the FGES (Fermi Gamma-ray Extended Source) and FHES (Fermi High-Latitude Extended Source Catalog), which are catalogs of extended sources only, and the FHL catalog (Fermi-LAT Catalog of Hard-Energy Sources), which is a catalog of high-energy sources only. These catalogs differ not only in the types of sources included, but also in the IRFs and Galactic emission models used, as well as in their time periods. Table 2 summarizes the characteristics of the previous FGL catalogs and other catalogs produced by Fermi-LAT.

2.2 Swift

The X-ray observation satellite Swift was launched in 2004 to detect and immediately observe gamma-ray bursts, which are high-energy phenomena, and to perform the first sensitive hard X-ray survey. It has a wide field of view

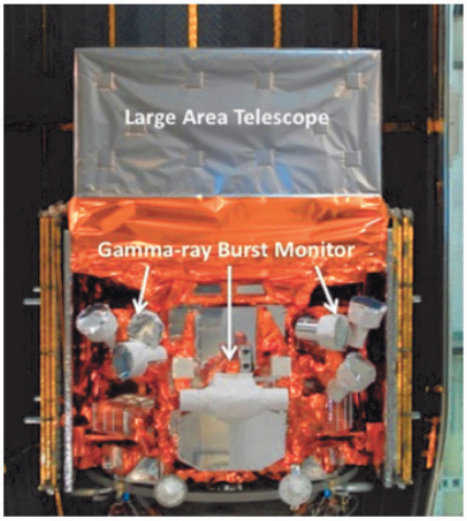

Figure 8: Position of Fermi detectors *Ref.* (8)

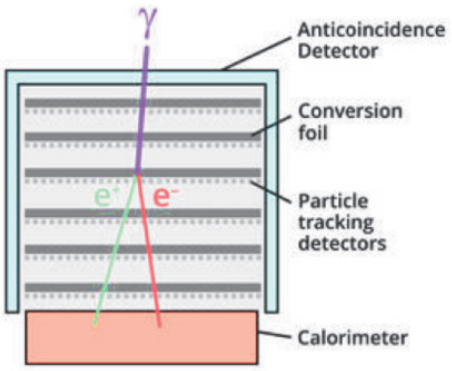

Figure 9: The structure of LAT*Ref.* (8)

Catalogs	IRFs/Galactic Radiation (diffuse) Model	Energy/Period	Number of Objects	Analysis
1FGL	P6_V3_DIFFUSE gll_iem_v02	0.1 - 100 GeV 11 months	1451(P)	Unbinned, F/B
2FGL	P7SOURCE_V6 gal_2yearp7v6_v0	0.1 - 100 GeV 2 years	1873(P)	Binned, F/B
3FGL	P7REP_SOURCE_V15 gll_iem_v06	0.1 - 300 GeV 4years	3033(P)	Binned, F/B
FGES	P8R2_SOURCE_V6 gll_iem_v06	10 GeV - 2 TeV 6 years	46(E)	Binned, PSF, $\|b\| < 7^\circ$
3FHL	P8R2_SOURCE_V6 gll_iem_v06	10 GeV - 2 TeV 7 years	1556(P)	Unbinned, PSF
FHES	P8R2_SOURCE_V6 gll_iem_v06	1 GeV - 1 TeV 7.5 years	24(E)	Binned, PSF, $\|b\| > 5^\circ$
4FGL	P8R3_SOURCE_V2 gll_iem_v07	0.05 GeV - 1 TeV 8 years	5064(P)	Binned, PSF
4FGL-DR2	P8R3_SOURCE_V2 gll_iem_v07	0.05 GeV - 1 TeV 10 years	5787(P)	Binned, PSF

Table 2: Fermi-LAT catalogsRef. (10)

and can perform observations flexibly and quickly. There are three detectors, UVOT, BAT, and XRT, each of which has a different detection energy band (Fig. 10). UVOT in the UV/visible energy band (170-650 nm) and is designed to observe the visible afterglow of gamma-ray bursts. BAT (Burst Alert Telescope) measures in the hard X-ray energy band of 15-150 keV. It uses the coded mask method for detection, which has high sensitivity and a wide field of view (2sr). This allows the BAT to provide the location of a gamma-ray burst within a few seconds of detection with an accuracy of about 3 arcmin. The last one is the XRT (X-ray Telescope), and I are analyzing the data obtained by the XRT in this study.

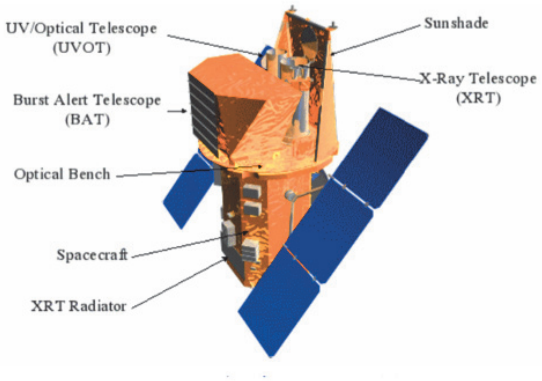

Figure 10: Swift

2.2.1 XRT

The probability of X-ray afterglow after a gamma-ray burst is considered to be more than 84%, and the XRT is a detector designed to observe this afterglow (Fig.11). When not observing gamma-ray bursts, the XRT can flexibly observe time-varying celestial objects many times. The detection energy band is 0.2-10.0 keV. The field of view of XRT and UVOT is narrower than that of BAT. In the case of XRT, the detector is a combination of an X-ray telescope and CCD, so the field of view is narrower at 23.6 arcmin. The role of XRT's GRB observations is to

Mirror	Wolter I (Focal length 3.5 m)
Detector	e2v CCD-22
	600 × 600 pixels
Pixel Size	40μm × 40μm
Readout Modes	Image(IM) mode
	Photodiode(PD) mode
	Windowed Timing(WT) mode
	Photon Counting(PC) mode
Pixel Scale	2.36 arcsec / pixel
FOV	23.6 × 23.6 arcmin
PSF	18 arcsec HPD @ 1.5 keV
	22 arcsec HPD @ 8.1 keV
Position Accuracy	3 arcsec
Time Resolution	0.14 μsec(PD), 1.8 μsec(WT), 2.5 sec(PC)
Energy Width	0.2 - 10 keV
Energy Resolution	140 eV @ 5.9 keV (at launch)
Effective area	~125 cm^2 @ 1.5 keV
	~20 cm^2 @ 8.1 keV
Sensitivity	2 × 10 $^{-14}$ erg cm^{-2} s^{-1} in 10^4 sec

Table 3: Performance of XRTRef. (12)

re-observe the location of gamma-ray bursts provided by BAT with an accuracy of a few arcmin and to narrow the localization of GRB to 5 arcsec within a few 100 seconds. The performance is summarized in Table 3 below.

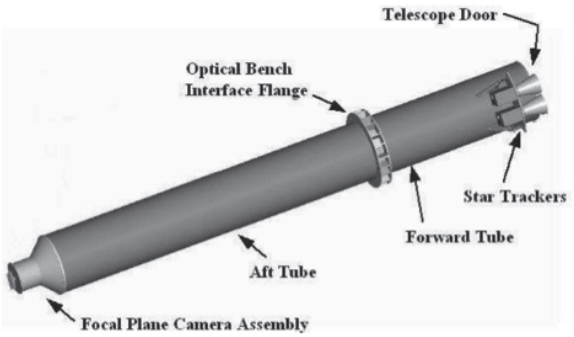

Figure 11: XRT detector

Since the Swift satellites are targeting gamma-ray bursts, they are required to quickly turn toward the target object. For this reason, the data acquisition process is automated (Figure 12) and follows a flowchart consisting of fmy modes after the target object has been observed. First, when the target object is observed, the precise location of the GRB is first acquired in the Image (IM) mode. Then, PD (Photodiode) mode, WT (Windowed Timing) mode, and PC (Photon counting) mode are executed in this order. In PD mode, no spatial information is obtained, but observation data is obtained with a time resolution of 0.14 ms, which is more accurate than PC and TW modes. The WT and PC modes produce one-dimensional and two-dimensional images, respectively. The PD, PC, and WT modes are changed according to the size of the flux, so the WT mode can be used to observe objects that would otherwise pile up in the PC mode. The X-ray data of radio galaxies used in this study were obtained with PC mode data.

Detector	EPIC MOS	EPIC PN	RGS	OM
Energy band	0.15 - 12.0 keV	0.15 - 15.0 keV	0.35 - 15.0 keV	160 - 600 nm
FOV	$30^{'}$	$30^{'}$	$\tilde{}5^{'}$	$17^{'}$
PSF(FWHM/HEW)	$5^{''}/14^{''}$	$6^{''}/15^{''}$	N/A	$\tilde{}1^{''}$
Pixel size	$40\mu m(1.1^{''})$	$150\mu m(4.1^{''})$	$81\mu m(9 \times 10^{-3}\mathring{A})$	$0.5^{''}$
Time resolution	$1.5ms$	$0.03ms$	$16ms$	$500ms$

Table 4: Detector performance of XMM-Newton

2.3 XMM-Newton

XMM-Newton is the largest scientific X-ray satellite by ESA (the European Space Agency), and it has 4-ton weight and 10 m height (Fig. 13). There are two X-ray detectors, EPIC (European Photon Imaging Camera) and RGS (Reflection Grating Spectrometer), and one optical detector, OM (Optical Monitor), which observe in 180-600 nm. And, EPIC has 2 detectors; one is MOS (Metal Oxide Semi-conductor), and the other is PN. MOS is front-side illumination type detector, and PN is back-side illumination type detector, thus PN has larger effective aria than MOS. I summarized about detectors of XMM-Newton below (Fig. 4).

3 Samples

In this study, I use gamma-ray emitting radio galaxies, thus these RGs are listed in 4FGL-DR2 based on the Fermi/LAT 10 years of observation data. This catalog contains 61 objects classified as MAGN (`RDG`, `rdg`, `AGN`, `agn`, `css`, and `ssrq`). The uppercase classes are the object which is identified with an other-wavelength counterpart by time variability study, and the objects of lowercase classes indicates associations with an other-wavelength counterpart in terms of just position. I analyzed X-ray data of Swift/XRT, which has an energy range of 0.5–10.0 keV, to study the time variation. Swift/XRT has observed more than 20 RGs in this catalog, and I chose the objects that there are more than 3 times available observed data by Swift/XRT PC mode in April 2019 to study robust time-variation. Therefore, 20 RGs are chosen as my sample RGs. The PC mode data contains 2-dimensional image information. Swift/XRT reprocessed data are downloaded from the UK Swift Science Data Centre[1]. This sample RGs are summarized on Table 1. The columns show the 4FGL name, common name, type of galaxy, redshift, gamma-ray flux, photon index, FR and HERG/LERG classifications taken from the literature, and inclination angle. In this sample, there are 7 FR-I/LERG objects, 9 FR-II/HERG objects, 1 FR-I/HERG object, and 3 unclassified objects. Some unclassified objects have other classes, for example, NGC 6328 is classified as the Compact symmetric object (CSO) and is also classified as a gigahertz-peaked spectrum (GPS) radio galaxy (Migliori et al. (2016)). The steady gamma-ray flux from NGC 6328 is produced in radio lobes (Migliori et al. (2016)), and GPS may be classified as a smaller version of FR-II objects (Principe et al. (2021), Tingay & Edwards (2015)). Therefore, I classify NGC 6328 into FR-II in this study. Cen A is also not classified obviously. Cen A could have a geometrically thick, optically thin, hot accretion flow like ADAF (Grandi et al., 2003). Thus, Cen A is classified as LERG in this study.

In addition, I use the RGs observed by XMM-Newton. This RGs are also in the 4FGL-DR2 catalog. Almost all XMM-Newton sample RGs in this catalog were not observed more than 3 times, thus this RGs could not be used for the study of robust time-variation. Therefore, I solely use this sample RGs to perform spectral analysis for the study about the relation between jet power and disk luminosity. I show this sample RGs on Table 4.1.1.

[1] https://www.swift.ac.uk/index.php

4 Analysis

4.1 X-ray analysis

4.1.1 Swift/XRT

I reprocess Swift/XRT data using `xrtpipeline` in the latest HeaSoft version 6.28. In addition, X-ray spectra and response files are created by `xselect`, `grppha`, and `xrtmkarf`. The source spectrum is extracted from the circular region, and a background spectrum is extracted from the annular region at 105–135 arcsec from the object. Occasionally, background radiation from hot gas in elliptical galaxies is present, and thus the background region is uniformly large in the sample RG. I find that X-ray data of 3C 111, 3C 120, and Cen A suffer from the pile-up. For such objects, I extract a source spectrum from the annular region at 9–50 arcsecs for 3C 111, 10–50 arcsecs for 3C 120, and 12–20 arcsecs for Cen A. I bin source spectra to contain at least 20 photon counts in each bin and apply χ^2 statistics in the spectral fitting for these spectra. However, lots of spectra data show few numbers of bins if they were binned. For these spectra, I bin at least 1 photon counts and apply the C-statistics in that case. I also do not sum the spectra. Spectral fitting is carried out for every observation of each object with `xspec` version 12.11.1. As a resolute, for 7 RGs, I applied the χ^2 statistic, where the reduced χ^2 is $0.8 < [\chi^2/\mathrm{bins}] < 1.2$ (Null hypothesis probability > 0.05). For the other 13 RGs, I applied the C-statistic is applied (Table 2). Most of the Swift/XRT observation is short duration, and thus not enough X-ray count spectra are available to apply a multicomponent model. Kayanoki & Fukazawa (2022) studied more detail X-ray spectral analysis of RGs listed in the 4FGL-DR2 catalog and showed that most 4FGL RGs can be fitted with the simple power-law model (`pegpwrlw`) with absorption. Therefore, I fit X-ray spectra by a single power-law model with the galactic absorption (`phabs*pegpwrlw` for all of my sample RGs, where (`pegpwrlw`) model can give the error of the X-ray flux adequately). I obtain galactic absorption by `nh` command in the `FTOOLS` and use fixed value in fitting. I calculated X-ray luminosity in 0.5–10 keV using `lumin` in `xspec` without including the absorption model.

For Cen A and 3C 111, these X-ray data is used in the energy range 3.0–10.0 keV and 1.5–10.0 keV, respectively. It is possible that local and/or intrinsic extra-absorptions affect the lower energy region of 3C 111 (Reynolds et al. (1998), Lewis et al. (2005), Ballo et al. (2011), Torresi (2012), Tombesi et al. (2013)), and also the core of Cen A has heavy absorption and other emission components (Grandi et al. (2003)). However, it is difficult to fit Swift/XRT spectra with a complicated model because of the insufficient photons. Therefore, I do not use the lower energy region and include extra absorption for 3C 111 and Cen A, `phabs*(phabs*pegpwrlw)`, considering extra absorption. Then I obtain an error-weight flux, power-law photon index, and luminosity averaged over all observations and their standard deviations for each galaxy. In Table 4.1.1, I present the results.

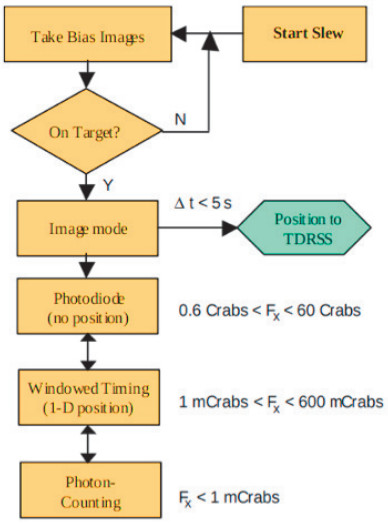

Figure 12: Detection flow of XRT

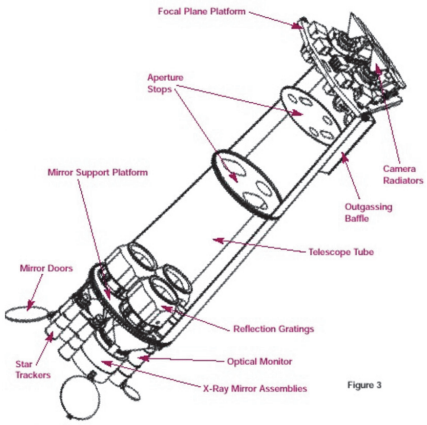

Figure 13: XMM-Newton?

Table 5: sample radio galaxies of Swift/XRT

4FGL name	Common name	type[a]	z	F_G^b	Γ_G^c	FR class	HERG/LERG	Reference[d]
				[10^{-12} erg cm^{-2} s^{-1}]				
4FGL J0013.6+4051	4C +40.01	agn	0.260	2.08±0.421	2.21±0.145	—	—	—
4FGL J0308.4+0407	NGC 1218	rdg	0.030	7.78±0.711	2.00±0.0641	I	LERG	C18,B10
4FGL J0312.9+4119	B3 0309+411B	rdg	0.134	4.10±1.03	2.47±0.193	II	HERG	B16,U18
4FGL J0316.8+4120	IC 310	RDG	0.019	2.85±0.676	1.78±0.178	I	LERG	A19,S19
4FGL J0322.6-3712e	NGC 1316/Fornax A	RDG	0.006	6.14±0.576	2.05±0.0659	I	LERG	A19,S19
4FGL J0418.2+3807	3C 111	rdg	0.050	16.0±1.33	2.71±0.0577	II	HERG[e]	A19,B10
4FGL J0433.0+0522	3C 120	RDG	0.034	13.0±1.13	2.72±0.0504	I	HERG[e]	A19,F15
4FGL J0519.6-4544	Pictor A	rdg	0.034	4.67±0.779	2.46±0.133	II	HERG	A19,S19
4FGL J0522.9-3628	PKS 0521-36	AGN	0.055	58.1±1.07	2.45±0.0141	II	HERG	D15,S19
4FGL J0840.8+1317	3C207	ssrq	0.680	3.89±0.511	2.48±0.0991	II	HERG	G10,S19
4FGL J1012.7+4228	B3 1009+427	agn	0.365	3.74±0.511	1.76±0.0879	II	—	A19,—
4FGL J1144.9+1937	3C 264	rdg	0.022	3.25±0.463	1.94±0.102	I	LERG	A19,B10
4FGL J1325.5-4300	NGC 5128/Cen A	RDG	0.002	63.8±1.58	2.65±0.0230	I	HERG	A19,F15
4FGL J1459.0+7140	3C 309.1	css	0.904	2.96±0.338	2.45±0.0936	II	HERG	S05,S19
4FGL J1516.5+0015	PKS 1514+00	rdg	0.053	4.48±0.649	2.59±0.114	I	LERG[f]	A19,DG83
4FGL J1630.6+8234	NGC 6251	rdg	0.020	12.6±0.669	2.35±0.0320	I	LERG	A19,S19
4FGL J1724.2-6501	NGC 6328	rdg	0.015	2.70±0.623	2.49±0.181	—	—	—
4FGL J1829.5+4845	3C 380	css	0.692	19.6±0.683	2.43±0.0295	II	HERG	S05,S19
4FGL J2156.0-6942	PKS 2153-69	rdg	0.028	3.54±0.578	2.83±0.110	II	HERG	A19,B16
4FGL J2334.9-2346	PKS 2331-240	agn	0.050	3.90±0.514	2.42±0.116	II	HERG	U18,U18

[a] Classification in 4FGL-DR2.

[b] Gamma-ray flux in 0.1–300 GeV.

[c] Gamma-ray photon index.

[d] References for radio (left) and optical (right) classification—A19:**?**; B16:Bassani et al. (2016); C18:Chiaro et al. (2018); D15:D'Ammando et al. (2015); DG83:Danziger & Goss (1983); F15:Fukazawa et al. (2015); S19:Stecker et al. (2019); U18:Ursini et al. (2018); B10:Buttiglione et al. (2010); G10:Gendre et al. (2010); S05:Shi et al. (2005).

[e] Objects classified as BLRG in **?**. We classify as HERG in this study.

[f] We classify this object as LERG because [OIII]/Hα is under 0.2 (Danziger & Goss (1983)).

Name	OBS-ID[a]	χ^2/C-stat	bin	c	dof	nhp	F_X	Γ_X
							$[10^{-12} ergcm^{-2}s^{-1}]$	
IC1531	0202190301	χ^2	20	95.8	110	0.831	0.451±0.0162	2.22±0.0534
PKS0625-35	0302440601	χ^2	30	364.2	386	0.781	7.64±0.0566	2.46±0.0112
NGC2484	0602390101	χ^2	30	133.2	137	0.577	0.269±0.00763	2.11134±0.0411
NGC315	0305290201	χ^2	20	243.0	226	0.209	1.07±0.0286	1.56±0.0550
B21113+29	0550270101	C-stat	10	103.4	84	0.00499	0.0962±0.0108	2.42±0.168

[a] The observation ID in XSA.

Table 6: Result of X-ray data analysis of XMM-Newton

4.1.2 XMM-Newton

I analysis X-ray data using SAS software. I use EPIC/PN data of XMM-Newton. I download observation data files (ODF) from XMM-Newton Science Archive (XSA) and calibrate these data by applying epchain command using current calibration files (CCF). EPIC detector needs to be considered about not only cosmic X-ray background (CXB), but also detector-derived flaring background. Thus, I create the event file by removing bright regions. And I define count rate < 0.5 counts/sec as Good Time Interval (GTI) in the light curve in the energy band between 10 keV and 12 keV, then I remove the period having counts rate over 0.5 as "flaring background" and create the filted event file file. I use this file for spectral files. For the spectral file, the central region is obtained according to the extent of the source in the image, and the background region is obtained and created as widely as possible. Pile-up must be taken into account for the XMM-Newton data, but the objects analyzed here are faint and thus I ignore the pile-up effect. For each source, flux and photon index are obtained by fitting the spectra with a single-powerlaw model multiplied by the Galactic absorption, and the results are summarized in Table 6.

4.2 Study of time variation using Hardness Ratio

Most of Swift/XRT observations are typically observed short period, thus X-ray spectra do not possess enough quality to study spectral variability. Therefore, I study the variation of hardness ratio instead of power-law photon index following Connolly et al. (2016). The definition of Hardness ratio is defined by following formula consisted of only the count rates of two energy bands, a soft count rate and a hard count rate, Hardness ratio = (H-S) / (H+S), where "H" means a count rate in the hard band of 2.0–10.0 keV, and "S" means a count rate in the soft band of 0.5–2.0 keV.

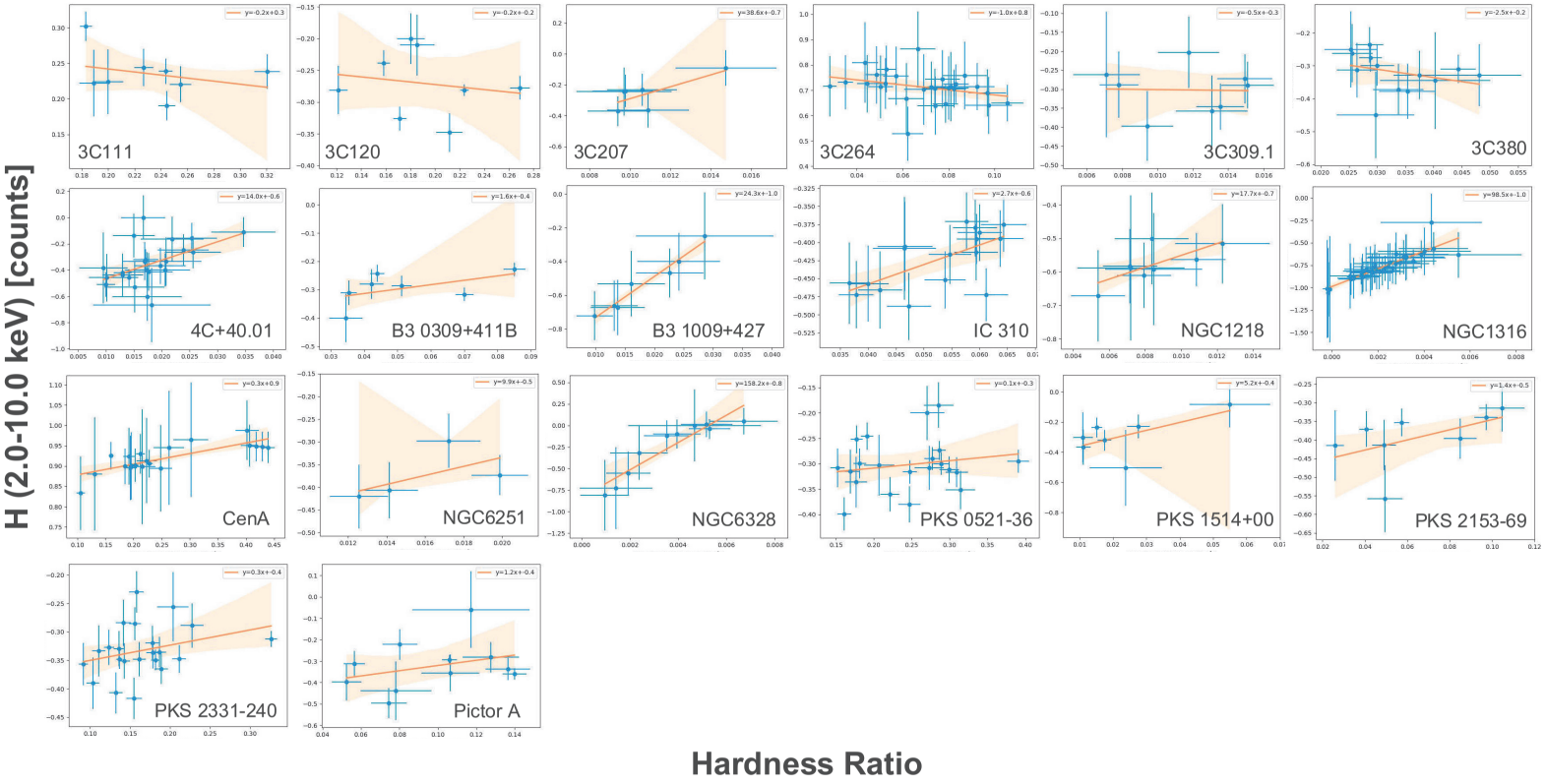

Figure 14: Scatter plot between hardness ratio and count rate in 2.0–10.0 keV. Data of NGC1316 and NGC6328 are not plotted. Blue dot data points correspond to one observation of Swift/XRT. Orange lines are a regression line, and orange regions show 95% confidence region. Parameters of these lines are summarized in table 2.

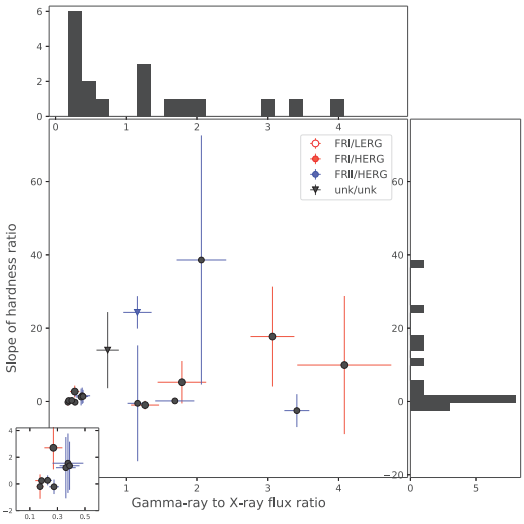

Figure 15: Relation between gamma-ray to X-ray flux ratio and slope of the relation between hardness ratio and count rate in 2.0–10.0 keV. Enlarged panel shows the region of the flux ratio in the range of 0.1–0.5 and the slope region in the range of -2.0–4.0. Top and right histograms represent projection. Red, blue, and black colors correspond to FR-I, FR-II, and unknown objects, respectively. Open circles, filled circles, and inverted triangles correspond to LERG, HERG, and unknown objects, respectively.

Following Connolly et al. (2016), Figure 1 shows the relationship between the hardness ratio and the count rate in the hard band for all observations of each galaxy, where regression lines are shown with a 95% confidence interval. For each object, the slope of regression lines is listed in Table .

4.3 Jet power estimation by SED model fitting using MCMC method

4.3.1 MCMC method

For estimation of kinetic jet power, I fit multi-wavelength Spectral Energy Distribution (SED) data with Synchrotron + Synchrotron self-Compton (SSC) model by using Markov-Chain Monte-Carlo (MCMC) method. Then I use the obtained parameters of Synchrotron + SSC model to estimate kinetic jet power. Here I use the algorithm developed in Yamada et al. (2020), and the program code used in this study was made available by Associate Professor Makoto Uemura of the Space Science Center, Hiroshima University[2]. In the MCMC method, the statistical model is fitted to the data according to the MCMC algorithm, resulting in a probability distribution for each parameter. The MCMC method is based on Bayesian statistics, and the resulting probability distribution is called the posterior distribution. In Bayesian statistics, the posterior distribution is estimated based on the likelihood and prior distribution. I defined a data as y_i, a dataset as $Y = y_1, y_2, ..., y_n$, estimating parameter as q, a probability distribution (posterior distribution) which obtained Y as $p(q|Y)$, a probability distribution giving q , which is equivalent to likelihood, as $p(Y|q)$, and a prior distribution of q as $p(q)$, then I can represent a posterior distribution,

$$p(q|Y) = \frac{p(Y|q)p(q)}{\sum_q (p(Y|q)p(q))}. \quad (1)$$

In the MCMC mechanism, random sampling is performed based on this posterior distribution to obtain the next posterior distribution, and eventually, a probability distribution is obtained. The MCMC algorithm is one of parameter estimation by maximum likelihood. In this study, the MCMC algorithm employs the applied Metropolis

[2]https://home.hiroshima-u.ac.jp/uemuram/yysscfit/

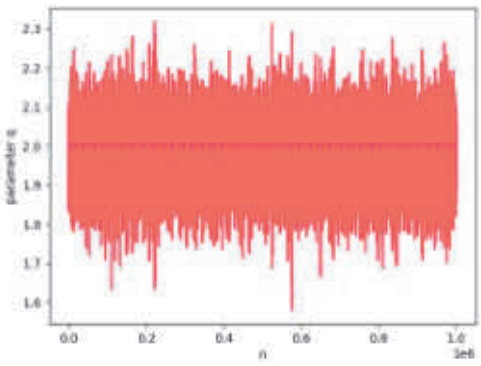

Figure 16: Trace plot of random sampling

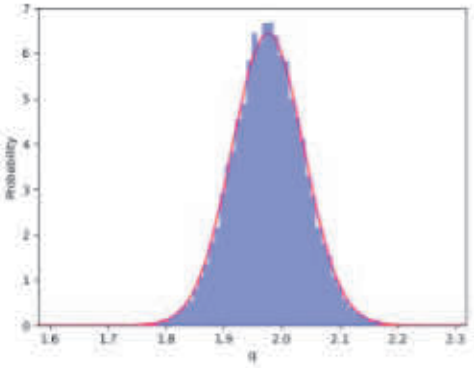

Figure 17: Histogram of figure16

method. In addition, the data are assumed to follow a normal distribution. The random sampling algorithm is as follows,

1. I define a candidate parameter set $q^{'}$, where the current parameter set q is given a random number.
2. I define P(q) as the product of the probabilities in all data by q and P(q') as the product of the probabilities in all data by q'. If the probability ratio P = P(q')/P(q) indicates more than 1, then the candidate parameter set q' is replaced by the parameter set q and recorded. In contrast, if P $<$ 1, the candidate parameter set is replaced by the candidate parameter set q' with probability P, and the parameter set is not updated with probability (1-P).

With this process, the obtained sampling data can be verified by trace plots and histograms (Figure 16, 17).

If a clear peak appears in the histogram of Figure 16, the sampling has converged and a result has been obtained, and the median and standard deviation of this peak is used as the result. Since multiple parameters are used in this study, corner plots will be created to check the correlation of each parameter as well as to confirm that each parameter is able to explore a sufficient parameter space. The Metropolis method does not use the initial step because the initial value can differ significantly from the final convergence value. For this reason, the study conducted 10^5 number of trials and basically did not use data from the first 10^4 trials.

4.3.2 data and model

The jet power estimation in this study uses multi-wavelength SED data, and the jet radiation model is fitted to multi-wavelength SEDs using MCMC methods to obtain the parameters necessary to calculate the jet power. Likelihood function to be maximized is defined Assuming that the flux data $f(\nu_i)$ in frequency ν_i with standard distribution σ_i in SED follow a normal distribution, the likelihood can be written on a logarithmic scale as follows,

$$\begin{aligned} \mathrm{logL} &= \log \prod_{\mathrm{i}=1}^{\mathrm{n}} \left(\frac{1}{\sqrt{2\pi\sigma^2}} \exp\left(-\frac{(\mathrm{f}(\nu_\mathrm{i}) - \mathrm{f}_{\mathrm{model}}(\nu_\mathrm{i}))^2}{2\sigma_\mathrm{i}^2} \right) \right) \quad (2) \\ &= C + \sum_{i=1}^{n} \frac{(f(\nu_i) - f_{model}(\nu_i))^2}{2\sigma_i^2} \quad (3) \end{aligned}$$

Here, the parameter C is $C = \sum_{i=1}^{n} \log(\frac{1}{\sqrt{2\pi\sigma_\mathrm{i}^2}})$, and this value is not depend on the variation of $f_{model}(\nu_i)$ and thus I just consider second term. When logL = 0, model $f_{model}(\nu_i)$ and flux data $f(\nu_i)$ are matched completely. Flux data from radio to ultraviolet energies were obtained from NASA/IPAC[3], X-ray data were obtained from

[3]https://ned.ipac.caltech.edu/

Swift/XRT or XMM-Newton/EPIC spectra I analyzed in 4.1.2, and 7 band flux data from the 4FGL catalog were used for the gamma-ray flux data. For hard X-ray flux data, I used the NuSTAR data for only those sources for which data were available in NuSTAR. MCMC method needs lots of time to estimate parameters if I use lots of data points. Thus, multi-wavelength flux data should be reduced as much as possible. For X-ray spectra, I binned them to several data points using the `grppha` command. The time epoch of NASA/IPAC data could be significantly different among data points. In this study, the NASA/IPAC data were used by assuming that RGs do not significantly change their spectra from the jet over a long period of time. The radio data has a larger scatter than the visible light data, and for this reason, the bin number was compiled to be around 5. The visible-light data were selected to be about 10 of them using the numpy.random module in python. UV data were not available for most of the objects, so only a few objects are used.

In this study, the Synchrotron+SSC model (referring Finke et al. (2008)) was used as the jet radiation model. The one-zone model is used for SSC. The main parameters used in this model are listed in the following table7.

Table 7: Main parameters of SSC

B	Magnetic field
δ	Doppler factor
$K_{\rm e}$	Normalization of electron
T	Time scale of time variability
$\gamma_{\rm break}$	Cut off Lorentz factor
p_0	Spectral index of electron (lower energy)
p_1	Spectral index of electron (higher energy)
γ_1	Lorentz factor (minimum)
γ_2	Lorentz factor (maximum)
z	Redshift

In optical band, I used the Swire template[4](Polletta et al. (2007)), which is a template for galaxy optical emission because most of the samples showed a component of emission from their host galaxies. This template is normalized at the flux of 5500$\mathring{A}$ and νF_ν values are fixed with respect to frequencies. Therefore, the coefficient t_{temp} is given as one of the parameters to estimate for the νF_ν of the template. There are 25 types in this template, including 3 ellipticals, 7 spirals, 6 starbursts, 7 AGNs (3 type I AGNs, 4 type II AGNs), and 2 composite (starburst+AGN). If the morphology of the object is specified by NASA/IPAC, the corresponding type is used; otherwise, Ell2, 2 Gyr aged elliptical galaxy, is used. I summarized Swire template type of each galaxy on Table 10. Although the accretion disk model should be introduced over the energy range from optical to X-ray, it is not used in this study because UV data obtained are poor and it is difficult to determine the model parameters using the MCMC method.

In parameter estimation using the MCMC method, results tend to converge when the SED data appears in the form of two peaks. For this reason, I classified the sample sources into three patterns based on the characteristics of the X-ray data on the SED. One is the case where the X-ray data has positive slope in the SED and can be explained by SSC radiation (pattern 1), and the second is the case where the X-ray data is has negative slope in the SED and can be explained by Synchrotron radiation (pattern 2). Finally, the X-ray radiation appears flat on the SED and is considered to be explained by the two components of Synchrotron and SSC (pattern 3). In this study, I estimate the parameters [B, δ, T, K_e, γ_{break}, p_0, p_1, t_{temp}]. For r_1 and r_2, which represent the Lorentz factor of emitting electrons at the minimum and maximum values of the Broken-power law of electron number density distribution, respectively, the lower and upper limits of these two parameters can be determined from the SED data and are fixed to $r_1 = 10$ and $r_2 = 10^9$ in this sample. For the three patterns, convergence experiments were conducted using ideal data to determine the initial conditions for each at analysis. In patterns 1 and 3, one parameter among $[B, \delta, T, K_e]$ is fixed and the other 7 parameters are kept free, then in pattern 2, 8 parameters are kept free. To fix one parameter among $[B, \delta, T, K_e]$, Time Scale of time variability is fixed at $T = 10^5$, considering that the Time scale of time variability of the RG spectrum is relatively moderate. If the results do not converge under the initial conditions, the parameters are fixed in the following order.

1. For Pattern 2 only, if no convergent result is obtained, fix at $T = 10^5$, as in patterns 1 and 3.

[4]This template data are downloaded from https://www.iasf-milano.inaf.it/ polletta/templates/swire_templates.html

2. The RG observed in Fermi is considered to be $\delta \lesssim 2$, so I fix it at $\delta = 1$

3. The next process is depending on the situation.

   (a) If most of the parameters are not converged, fix the parameter t_{temp} for the coefficients of the template. This makes it easier to determine the position of the peak by the Synchrotron of the jet.

   (b) If there is no or little data at the right hem of the peak of the Synchrotron and SSC models, i.e., no or little gamma or UV data, a situation can occur where only the p_1 parameter cannot be determined. In this case, it is impossible to determine p_1 unambiguously but attempt convergence by giving a prior distribution. p_1 is given as a minimum value of 0 and a maximum value of 20, and if it diverges to the maximum value, a median value of $\mu = 12.0$ and $sigma = 2.0$ are given so that p_1 can take data in the range of 2-20 with 4σ.

4. If no convergent results could be obtained up to this point, I fixed $p0 = 2.4$ and $p1 = 4.8$ and attempted convergence. There is no basis for these values; they are determined empirically.

4.3.3 Jet Power estimation

The timescale of time variation T is the timescale of the shortest time scale observed in the observer's frame. The timescale T' in the co-moving frame is defined by the speed of light c and the radius of the emission region R'_b.

$$T' \geqq \frac{R'_b}{c} \tag{4}$$

Therefore, the timescale T of the time variation in the observer frame is limited as in equation (5).

$$T' \geqq T = \frac{(1+z)R'_b}{\delta c} \tag{5}$$

Therefore, I can say that the timescale represents the size of the radiating region. Defining the electron mass m_e, the electron charge e, the Planck constant h, the magnetic field in the radiating region B, and the Lorentz factor $gamma$ of the electron in jet, the dimensionless radiation energy of a photon in the observer's system is $\epsilon = \frac{h\mu}{m_e c^2}$. I define the following x and $R(x)$ using these parameters.

$$x = \frac{4\pi\epsilon' m_e^2 c^3}{3eB} \tag{6}$$

$$R(x) = \frac{x}{2}\int_0^{\frac{\pi}{2}} d\theta \sin\theta \int_{\mathrm{x/sin}\theta}^{\infty} \mathrm{dtK_{5/3}(t)} \tag{7}$$

The $K_{5/3}$ is a Bessel function. This function $R(x)$ can be approximated as follows depending on the range of x.

$$\log(R) = A_0 + A_1 y + A_2 y + A_3 y + A_4 y + A_5 y \quad (10^{-2} < x < 10, \quad y = \log(x)) \tag{8}$$

$$R(x) = \begin{cases} 1.808242 x^{1/3} & (x \ll 1) \\ \frac{\pi}{2} e^{-2}\left(1 - \frac{99}{162x}\right) & (x \gg 1) \end{cases} \tag{9}$$

Equation (9) is an approximation by **?**. The values of the coefficients $[A_0, A_1, A_2, A_3, A_4, A_5]$ of the (8)formula are summarized in the following table (8). The synchrotron emissivity of isotropic electrons in a non-uniform magnetic field is given by

$$\epsilon' J'_{syn}(\epsilon') = \frac{\sqrt{3}\epsilon' e^3 B}{h}\int_1^{\infty} d\gamma' N'_e(\gamma') R(x), \tag{10}$$

and the flux and intensity of synchrotron radiation are given by

$$f_\epsilon^{syn} = \frac{\delta_D^4 \epsilon' J'_{syn}}{4\pi d_L^2} = \frac{\sqrt{3}\delta^4 \epsilon' e^3 B}{4\pi h d_L^2}\int_1^{\infty} d\gamma' N'_e(\gamma') R(x) \tag{11}$$

$$I_{syn} = \int_{\delta\epsilon_B\gamma'_1/(1+z)}^{\delta\epsilon_B\gamma'_2/(1+z)} d\epsilon \frac{f_\epsilon^{syn}}{\epsilon^{3/2}}. \tag{12}$$

Coefficients	$10^{-2} < x < 10^{0}$	$10^{0} < x < 10^{1}$
A_0	-0.35775237	-0.35842494
A_1	-0.83695385	-0.79652041
A_2	-1.1449608	-1.6113032
A_3	-0.68137283	0.26055213
A_4	-0.22754737	-1.6979017
A_5	-0.031967334	0.032955035

Table 8: Coefficients of the equation Finke et al. (2008)

In this equation, d_L is the luminosity distance, which defines the degree of decrease in the brightness of a object by its distance. Assuming z for the redshift, H_0 for the Hubble constant, Ω_Λ for the dark energy density parameter, and Ω_m for the total matter density parameter, the luminosity distance can be written as follows for a general flat universe with a cosmological constant.

$$d_L = \frac{1+z}{H_0} \int_0^z \frac{dz}{\sqrt{\Omega_m (1+z)^3 + \Omega_\Lambda}} \tag{13}$$

Assuming that the electron number density follows a broken power law distribution such that the power index changes from $p0$ to $p1$ at a certain Lorenz factor value γ_{break} (ref. Figure 18), electron number density is explained following equitation (14) using the electron at the minimum Lorenz factor γ_1 and maximum Lorentz factor γ_2 and the Heaviside function.

$$N_e(\gamma) = K_e \left[\left(\frac{\gamma}{\gamma_{break}} \right)^{-p_0} H(\gamma_{break} - \gamma) + \left(\frac{\gamma}{\gamma_{break}} \right)^{-p_1} H(\gamma - \gamma_{break}) \right] H(\gamma; \gamma_1, \gamma_2) \tag{14}$$

Heaviside function is similar to step function and shows the following properties.

$$H(x) = \begin{cases} 1 & (x > 0) \\ 0 & (x < 0) \end{cases} \tag{15}$$

$$H(x; x_1, x_2) = \begin{cases} 1 & (x_1 < x < x_2) \\ 0 & (otherwise) \end{cases} \tag{16}$$

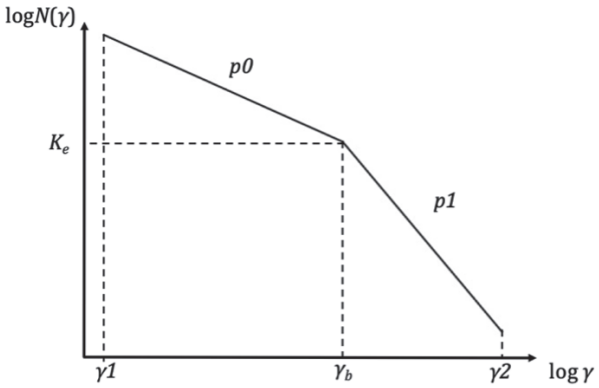

Figure 18: broken-power-law distribution of electron

Based on the above calculations, I consider inverse Compton scattering. Considering the synchrotron radiation flux, taking into account the photon number density and radiation energy density of the synchrotron, the inverse

Compton scattering emissivity for an isotropic and uniform photon and electron distribution is integrated over the entire volume and is expressed as follows.

$$\epsilon' J'_{SSC}(\epsilon) = \frac{9\sigma_T d_L^2 \epsilon_s'^2}{4\delta_D^4 R_b'^2} \int_0^\infty d\epsilon' \frac{f_\epsilon^{syn}}{\epsilon'^3} \int_{\gamma'_{min}}^{\gamma'_{max}} d\gamma' \frac{N'_e(\gamma')}{\gamma'^2} Fc(q, \Gamma_e) \tag{17}$$

The flux of the scattering component of the observed inverse Compton scattering can be expressed by the following equation.

$$f_{\epsilon_s}^{SSC} = \frac{\delta_D^4 \epsilon'_s J'_{SSC}(\epsilon)}{4\pi d_L^2} = \frac{9}{16} \frac{(1+z)^2 \sigma_T \epsilon_s'^2}{\pi \delta_D^2 c^2 t_{v,min}^2} \int_0^\infty d\epsilon' \frac{f_\epsilon^{syn}}{\epsilon'^3} \int_{\gamma'_{min}}^{\gamma'_{max}} d\gamma' \frac{N'_e(\gamma')}{\gamma'^2} Fc(q, \Gamma_e) \tag{18}$$

In Equation 17 and 18, T is the timescale of the time variation in the observer frame shown in Equation 5, ϵ_s is the energy of the scattered photon, and σ_T is the Thomson scattering cross section. In addition, $Fc(q, \Gamma_e)$ is the Compton scattering kernel, which represents the effect of inverse Compton scattering in the case of isotropic photon and electron distributions.

$$Fc(q, \Gamma_e) = \left[2q\mathrm{lnq} + (1+2\mathrm{q})(1-\mathrm{q}) + \frac{1}{2} \frac{(\Gamma_\mathrm{e}\mathrm{q})^2}{1+\Gamma_\mathrm{e}\mathrm{q}} (1-\mathrm{q}) \right] H(q; \frac{1}{4\gamma'^2}, 1) \tag{19}$$

The q and Γ_e in the equation are as follows.

$$q \equiv \frac{\epsilon'/\gamma'}{\Gamma_e(1-\epsilon'_s/\gamma')} \tag{20}$$

$$\Gamma_e = 4\epsilon'\gamma' \tag{21}$$

The total energy radiation rate of the jet can then be obtained as the sum of the energy radiation rate of all particles and the energy radiation rate of the magnetic field. Here, the respective energies of the electron and magnetic field can be written as in the following equations (22) and (23), respectively. The electron energy can be transformed as in equation (24) using equations (12) and (11) for the total energy of synchrotron radiation.

$$W'_B = \frac{R'^3 B^2}{6} \tag{22}$$

$$W'_e = m_e c^2 \int_{\gamma'_1}^{\gamma'_2} d\gamma' \gamma' N'_e(\gamma') \tag{23}$$

$$= m_e c^2 \frac{6\pi d_L^2}{c\sigma_T \epsilon_B^2 U_{B,cr} \delta^4} \frac{1}{2} \sqrt{\frac{\delta\epsilon_B}{1+z}} I_{syn} \tag{24}$$

$U_{B,cr}$ represents the energy density $U_{B,cr} = B_{cr}^2/8\pi$ of the critical magnetic field B_{cr} in the co-moving frame, where the critical field is $B_{cr} = 4.414 \times 10^{13}$G Finke et al. (2008). From these energies the jet power is estimated by the following (**??**), (25), (26) equations.

$$P_\mathrm{B} = 2\pi R_b'^2 \beta \Gamma^2 c \frac{W'_B}{V'_b} \tag{25}$$

$$P_\mathrm{e} = 2\pi R_b'^2 \beta \Gamma^2 c \frac{W'_e}{V'_b} \tag{26}$$

The V'_b represents the volume $V'_b = \frac{4\pi R_b'^3}{3}$ at radius R'_b of the radial extent (blob) in the comoving frame. Also Γ is the Lorentz factor, $\Gamma = (1-\beta^2)^{-1/2}$. With viewing angle *theta*, the Doppler factor $\delta \equiv 1/[\Gamma(1-\beta cos\theta)]$. Assuming a relativistic velocity, then $sin\theta \backsim 1/\Gamma$ due to the beaming effect, and therefore $\delta \backsim \theta$.

For the cold proton number density in jet, I assume that there is one cold proton per radiating electron in the jet (Ghisellini et al. (2014)). Thus, the comoving energy in the protons is given the following equation.

$$W'_p = m_p c^2 \int_{\gamma'_1}^{\gamma'_2} d\gamma' N'_e(\gamma') \tag{27}$$

$$P_p = 2\pi R_b'^2 \beta \Gamma^2 c \frac{W'_p}{V'_b} \tag{28}$$

In this study, the kinetic jet power is calculated from Ghisellini et al. (2014),

$$P_{\rm jet} = P_{\rm rad} + P_{\rm B} + P_{\rm e} + P_{\rm p}. \tag{29}$$

$P_{\rm rad}$, $P_{\rm B}$, $P_{\rm e}$, and $P_{\rm p}$ are the power of radiation, magnetic field, electron, and proton, respectively. The $P_{\rm rad}$ can be expressed by the following equation using the bolometric luminosity L_{jet}^{bol} and Lorentz factor Γ, which can be estimated from the multi-wavelength SED.

$$P_{\rm rad} = 2 f L_{\rm jet}^{\rm bol} \frac{\Gamma^4}{\delta^6} \tag{30}$$

Factor 2 implies a jet in both directions. In this study, f = 16/5 is applied to consider the Synchrotron +SSC model (Ghisellini et al. (2014)). If $P_{\rm rad}$ is the entire kinetic power of the jet, it would use all the energy to produce the observed radiation, and the jet would stop. However, VLBI observations show that the jet continues to move away from the BH at a distance of 1 pc (Ghisellini et al. (2014)). Therefore, $P_{\rm rad}$ is the exact lower limit of the jet, which I define as $P_{\rm jet}$ by adding the magnetic field and the power of the electrons and protons. And also, it is considered that $P_{\rm rad}$ is 10 % of $P_{\rm jet}$ in AGN and Gamma-ray burst (Nemmen et al. (2012)). In this study, I often fix Doppler factor $\delta = 1.0$ in estimation by MCMC method, and I use the fixed value of Lorentz factor $\Gamma = 10.0$. Therefore, I consider $P_{\rm rad}$ to be overestimated, and thus I don't use $P_{\rm rad}$ to calculate $P_{\rm jet}$ in Eq. (29). The magnetic field power $P_{\rm B}$ is a part of the gravitational potential energy of the material falling into the BH in the accretion disk, which amplifies the magnetic field and converts a part of the huge stored energy of the BH rotation energy into the dynamical jet power (Ghisellini et al. (2014)).

5 X-ray properties of Gamma-ray emitting RGs

5.1 X-ray properties

Figure shows the relation between the slope of the regression line of Figure and the gamma-ray to X-ray flux ratio. Moreover, FR and HERG/LERG classifications are applied in Figure. Some objects are concentrated on the lower left-hand side and other objects are located on the right-hand side. Therefore, I classify them into two groups; Group A has a gamma-ray to X-ray flux ratio greater than 0.5, whereas Group B has a gamma-ray to X-ray flux ratio less than 0.5. For Group A, the slope of the hardness ratio distributes broadly. Whereas, for Group B, that distributes only at small values less than 5.0. It means that Group A shows a strong harder-when-brighter or a weak softer-when-brighter trend, with a higher gamma-ray flux than that of the X-rays. In contrast, Group B shows a weak harder-when-brighter or a weak softer-when-brighter trend, with a lower gamma-ray flux than that of the X-rays. Group A is composed of FR-I/LERG and FR-II/HERG, whereas Group B is composed of FR-I/HERG, FR-II/HERG, and FR-I/LERG objects. The FR-I/LERG objects of Group B are Cen A and IC 310.

Figure shows the relationship between the X-ray photon index and the gamma-ray photon index with FR and HERG/LERG classifications. In Figure, I classified two groups. Group α shows a photon index of >1.8 in X-ray and <2.1 in gamma-ray on the upper left-hand side in Figure. Group β shows a photon index of <1.8 in X-ray and >2.1 in gamma-ray on the lower right-hand side in Figure. I confirmed that Group α is mainly composed of FR-I/LERG objects, and Group β have FR-I/LERG objects. On the other hand, all FR-I/HERG and FR-II/HERG objects are in Group β only.

In addition, I calculated the Eddington luminosity ratio in the X-ray band for my sample RGs. I used the BH mass from the literature shown in Table 3, and I calculate the BH mass of the objects whose BH mass is not available, according to the following formula Graham (2007),

$$\log(M_{BH}/{\rm M}_\odot) = -0.37(\pm0.04)(M_K + 24) + 8.29(\pm0.08). \tag{31}$$

M_K is the K-band absolute magnitude and determined from the apparent magnitude in the 2MASS All-Sky Point Source Catalog. Figure 4 shows the histogram of the ratio of X-ray luminosity to Eddington luminosity. In Figure 4, FR-I/LERG objects have a smaller Eddington luminosity ratio of $< 10^{-3}$, while FR-II/HERG objects have high values of $> 10^{-3}$, except for Pictor A. In the case of FR-I/HERG, 3C 120 shows a ratio of $> 10^{-3}$ as in FR-II/HERG.

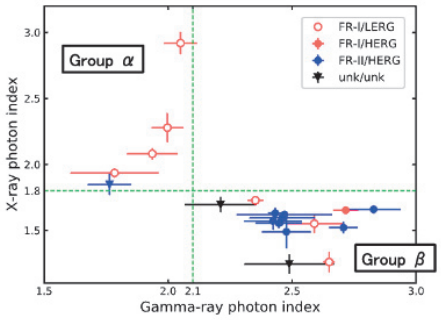

Figure 19: The relation between X-ray Photon Index and gamma-ray Photon Index

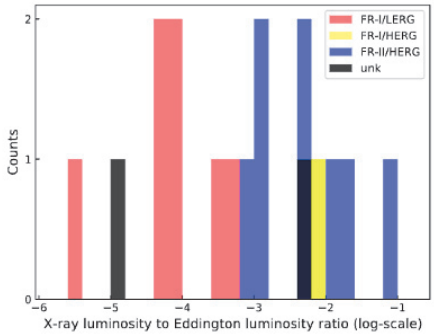

Figure 20: The histogram of X-ray luminosity to Eddington luminosity ratio

5.2 Classify X-ray origins

I suggest a trend that Group A consists of FR-I/LERG and FR-II/HERG and shows a strong harder-when-brighter trend or a weak softer-when-brighter trend with a higher gamma-ray to X-ray flux ratio, whereas Group B consists of FR-I/HERG, FR-II/HERG, and FR-I/LERG where FR-I/LERG are Cen A and IC 310, and shows a weak harder-when-brighter or weak softer-when-brighter trend with lower gamma-ray to X-ray flux ratio. According to Connolly et al. (2016), Seyfert galaxies have a harder-when-brighter trend when the accretion disk is formed similar to ADAF and a softer-when-brighter trend when the accretion disk is formed similarly to standard disks. It is believed that Seyfert galaxies is emitted from their disk/corona in X-ray, whereas RGs is emitted from not only their disk/corona but also from the jet in X-ray. I consider that if the accretion disk is formed similarly to the ADAF and its emission is weak in X-rays, the jet emission will be observed more strongly in X-rays than the disk/corona emission. Such a case corresponds to a low mass accretion rate $\dot{m}$; according to the relation between the jet power and the accretion rate (Ghisellini et al. (2014)), the ADAF emission is proportional to $\dot{m}^2$ while Jet emission is considered to be $\propto \dot{m}$, leading to relatively weak ADAF emission compared to jet emission. Thus, such RGs have a strong harder-when-brighter trend, which is a typical feature of Blazars where jet radiation is dominant. In addition, if an accretion disk is formed in the same way as a standard disk, both the jet and the disk/corona radiation contribute to the X-ray emission because the disk/corona emission is $\propto \dot{m}$. Thus, a softer-when-brighter trend of standard disk emission weakens the harder-when-brighter trend of the jet. As a result, a weak harder-when-brighter trend or a weak softer-when-brighter trend is observed for such RGs.

Based on this interpretation, accretion-efficient HERG objects show a weak softer-when-brighter or a weak harder-when-brighter trend. In Figure 1, HERG objects show a slope value less than 2.0, except for 2 HERG objects that exhibit much larger slope values than the other HERG objects. However, they are contained in both

Group A and Group B. It is possible that this depends on the relative ratios of jet to disk/corona emission leading to different flux ratios of gamma rays to X-rays. Therefore, Group B with a small flux ratio of gamma rays to X-rays indicates that disk/corona radiation is dominant in X-rays, while Group A indicates that jet radiation is dominant in X-rays. It is possible that the X-ray spectrum is absorbed by the torus surrounding the central region. According to some papers (Chiaberge et al. (2002), Balmaverde et al. (2006), Baldi et al. (2010)), FR-I objects do not have a torus and FR-II objects do. FR-II is a board line RG (BLRG) if the object is observed face-on, and FR-II is a narrow line RG (NLRG) if the object is observed edge-on. Thus, if FR-II is BLRG, the torus absorption is negligible. In addition, some papers have interpreted the RGs observed in Fermi, including FR-I and FR-II, as having a small inclination angle due to the torus and negligible intrinsic absorption (Pushkarev et al. (2017), Kayanoki & Fukazawa (2022)). Therefore, the intrinsic absorption due to the torus was neglected, and the relationship between the X-ray spectrum and the tilt angle was not found.

Cen A and IC 310, the FR-I/LERGs of Group B, deviate from this interpretation. Cen A is reported to exhibit a Fe-Kα line at 6.4 keV (Grandi et al. (2003), Evans et al. (2004)). The presence of Fe-Kα lines can be interpreted as the formation of a standard accretion disk. For Cen A, however, Grandi et al. (2003) reported results that denied the standard cold thin disk and suggested other possibilities such as ADAF or structured jet emission, and Meisenheimer et al. (2007) reported the possibility that the Cen A disk could form like an ADAF. On the other hand, IC310 is observed in the TeV gamma-ray band, suggesting that jet radiation is dominant over multiple wavelengths. Furthermore, Aleksić et al. (2014), which analyzed X-ray data from Chandra, XMM-Newton, and Swift/XRT observed between 2003 and 2007, showed lower X-ray flux than the present study. Since the data used in this study were mainly observed in 2012, it is possible that the X-ray data in this study correspond to accidentally bright conditions and that the appropriate X-ray data show gamma ray to X-ray flux ratios higher than 0.5. Therefore, IC 310 is treated as an exception to Figure 1 in this study.

I also suggested a trend that the Group α shows a photon index of >1.8 in X-ray and <2.1 in gamma-ray, most of which are FR-I/LERG and the Group β shows a photon index of <1.8 in X-ray and >2.1 in gamma-ray and is composed of FR-I/HERG and FR-II/HERG, except for 3 FR-I/LERG objects. This can be explained from Figure 5, which shows the trend in spectral energy distribution (SED) for these two groups. The left side of Figure 5 shows the SED corresponding to the α group, where the two peaks are located on the high energy side, resulting in a soft spectrum in the X-ray band and a hard spectrum in the gamma band. The right side of Figure 5 shows the SED corresponding to the β group; the two peaks are not located on the high energy side, resulting in a spectrum that is hard in the X-ray band and soft in the gamma band.

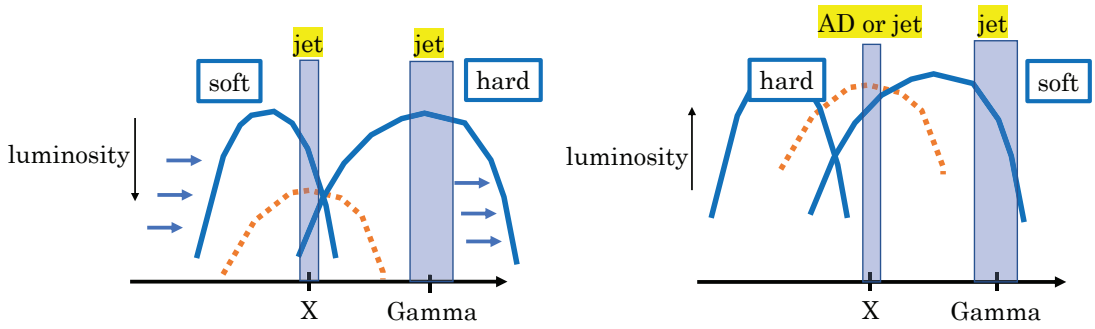

Figure 21: SED model

The RGs on the left part of Figure 4 are FR-I/LERG, and they show a low Eddington luminosity ratio and thus a lower accretion rate $\dot{m}$. In this case, as discussed above, the disk/corona emission is relatively weaker than the jets emission in the X-ray band. A large slope in X-ray band of these RGs indicates that the X-ray band corresponds to the synchrotron tail, similar to the case of BL Lac objects whose two SED peaks lie at higher energies. This is consistent with the scenario that FR-I RGs belong to the parent population of BL Lac objects.

On the other hand, the RGs on the right part of Figure 4 are FR-II/HERG, and they have a high Eddington luminosity ratio and thus a higher accretion rate $\dot{m}$. In this case, the jet and disk/coronal emission may have

Summary of suggestions of dominant X-ray emission components and other properties of my sample radio galaxies

Name	FR type	HE/LE	Result $1a^0$ slope vs Flux ratio	Result $2b^0$ photon index relation	Result 3 c^0 mass accretion rate
NGC 1218	I	LERG	jet	jet	low
NGC 1316	I	LERG	jet	jet	low
3C 264	I	LERG	jet	jet	low
B3 1009+427	II	unk	jet	jet	high
B3 0309+411B	II	HERG	disk/corona	disk/corona	high
3C 111	II	HERG	disk/corona	disk/corona	high
3C 120	I	HERG	disk/corona	disk/corona	high
PKS 2153-69	II	HERG	disk/corona	disk/corona	high
PKS 2331-240	II	HERG	disk/corona	disk/corona	high
Pictor A	II	HERG	disk/corona	disk/corona	low
NGC 5128(Cen A)	I	LERG	exception	disk/corona	low
PKS 1514+00	I	LERG	jet	disk/corona	low
NGC 6251	I	LERG	jet	disk/corona	low
NGC 6328	II	unk	jet	disk/corona	low
IC 310	I	LERG	exception	jet	low
4C +40.01	unk	unk	jet	disk/corona	high
PKS 0521-36	II	HERG	jet	disk/corona	high
3C 207	II	HERG	jet	disk/corona	high
3C 309.1	II	HERG	jet	disk/corona	high
3C 380	II	HERG	jet	disk/corona	high

a^0

Results of Figure 2. "jet" and "disk/corona" correspond to Group A and Group B, respectively.
b^0 Results of Figure 3. "jet" and "disk/corona" correspond to Group α and Group β, respectively.
c^0 Results of Figure 4. "high" or "low" represent the X-ray Eddington luminosity ratio of higher or less than 10^{-3}, respectively.

equivalent fluxes observed, and thus neither appears to be prominent. The hard X-ray slopes of these RGs do not allow us to distinguish between a jet or a disk/corona in X-ray band, but the soft gamma-ray slopes of these RGs indicate that the gamma-ray band corresponds to the low-energy tail of the SSC, similar to the case of FSRQ objects whose two SED peaks lie at low energies. This is consistent with the scenario that FR-II RGs belong to the population of FSRQ sources. For the FSRQ, thermal emission photons enter the jet from the disk/corona, broadline region, and dust, thus the external Compton (EC) model is applied to its SED model (Zacharias & Schlickeiser (2012)). Fukazawa et al. (2022) studied gamma-ray emitting radio galaxies detected by Fermi, including my sample, and compared the peak luminosity ratios of two SEDs, FSRQ and RG, and showed that the peak luminosity of the X-ray to gamma-ray SED is equal to or lower than the synchrotron peak luminosity. Therefore, the EC model is not addressed in this paper.

I considered the X-ray origin of the RGs based on their hardness ratio, photon index, Eddington luminosity ratio, and optical and radio classification. Based on the X-ray characteristics of hardness ratio and photon index, the gamma-ray emitting sample RGs were classified into three types in terms of X-ray origin, as shown in Table 5.2.

One is RGs classified as Group A and Group α. This type of RG is considered to have jet emission predominantly in the X-ray band. The second is RGs classified in Group B and Group β. RGs classified as Group B and Group β are considered to have disk/coronal emission strongly observed in the X-ray band. The third is RGs that are not classified into the above two types. This type of RG is considered to have neither jet nor disk/coronal emission dominant in the X-ray band.

In the following, I refer to them as the jet-dominant RG, disk/corona-dominant RG, and intermediate RG, respectively.

As can be seen in Figure 4, the jet-dominant type of RG suggests a low accretion rate. This is consistent with the fact that RGs of this type are FR-I/LERGs, with the exception of B3 1009+427. In addition, the X-ray Eddington

luminosity ratio is indeed low at $< 10^{-3}$. In contrast, it is suggested that the disk/corona-dominant type RGs have a higher accretion rate. This is consistent with the fact that RGs of this type are FR-II/HERGs, with the exception of Cen A. Note that the above classification is based solely on X-ray photon index, time variability, and gamma-ray to X-ray luminosity ratio, but can indicate the Eddington luminosity ratio and the origin of the X-ray radiation.

However, the above classification does not fully correspond to the Eddington luminosity ratio or the origin of X-ray radiation, thus leaving intermediate RGs. Most intermediate-type RGs tend to be " harder-when-brighter" and are considered to have a jet origin because of their large gamma-ray to X-ray flux ratios, whereas the harder X-ray spectra suggest a disk/corona origin. However, the hard X-ray spectrum is also described by the low energy tail of the jet SSC radiation and the low Eddington luminosity ratio (i.e., low mass accretion rate), leading to faint disk/corona emission. Therefore, it is possible that these RGs have jet-dominated X-ray emission, but unlike jet-dominant RGs, the SED peak of the jet emission is low, leading to hard X-ray spectra and soft GeV gamma-ray spectra.

Further examination of the Eddington luminosity ratios of intermediate RGs reveals the presence of both high luminosity ratio RGs and low luminosity ratio RGs. Intermediate RGs with low Eddington luminosity ratios of $< 10^{-3}$ consist only of FR-I/LERGs, while those with high Eddington luminosity ratios consist of FR-II/HERGs, except for unclassified sources. For the former, PKS 1514+00, NGC 6251, and NGC 6328, the SED peak of the jet would be at a lower energy despite the lower Eddington luminosity ratio, and thus does not apply to the scenario in Figure 5. In the latter case, 4C +40.01, PKS 0521-36, 3C 207, 3C 309.1, and 3C 380 are classified as `CSS`, `SSRQ`, and `AGN` in 4FGL-DR2. CSS and SSRQ show intermediate properties between FR-II and FSRQ and are fairly bright sources. PKS 0521-36 is also a very bright object among the RGs classified as `AGN` in 4FGL-DR2. In this study, I treated CSS and SSRQ as FR-II, but these are more luminous objects than FR-II. Therefore, the jet emission from CSS and SSRQ is very bright and the disk/coronal emission is possibly buried in the jet emission.

6 The relationship between jet power and disk luminosity

6.1 Jet power estimation by radio luminosity

For the jet power calculations, I used 151 MHz Luminosity (Willott et al. (1999)).

$$P_{\rm jet} = 9.5 \times 10^{46} \left(\frac{f}{10}\right)^{3/2} \left(\frac{L_{\rm 151MHz}}{10^{28}\ {\rm W\ Hz^{-1}\ sr^{-1}}}\right)^{6/7} \quad [\ {\rm erg\ s^{-1}}] \tag{32}$$

The parameter f includes several effects: an energy loss component due to adiabatic expansion of the jet, a component due to the bulk and turbulent kinetic energy of the lobe, the ratio of the energy of the radiating material to $P_{\rm jet}$, the angle between the line of sight and the magnetic field, the low-frequency cutoff in the synchrotron spectrum, the volume-filling factor, and the dissipation from the minimum energy state (Inoue et al. (2017)). The jet power is calibrated by including several factors such as the cutoff of the synchrotron spectrum at low frequencies, the volume-filling factor, and the dissipation from the minimum-energy condition. Willott et al. (1999) used an X-ray cavity, which gave a constraint of $1 \leq f \lesssim 20$. Inoue et al. (2017) used $f = 10$ from the study of X-ray cavity and hot spot. This f value is assumed to be a fixed value ($f = 10 - 20$) (Martínez-Sansigre & Rawlings (2011), Fernandes et al. (2011), Hardcastle et al. (2007)), and then I assumed $f = 10$. In addition, I note that this calculation of jet power was obtained from the correlation O_{II} narrow line luminosity which is a proxy of jet power and L_{151}, and it has large uncertain and strongly depends on the sample (Hardcastle et al. (2009), Fernandes et al. (2011)). Since NASA/IPAC could not provide sufficient 151 MHz data, the 1.4 GHz data is transformed to 151 MHz flux using the assumption of $F_\nu[{\rm Jy}] \propto \nu^{-\alpha}$. The spectral index was set to $\alpha = 0.8$ (Inoue et al. (2017)). The jet power obtained from Eq.(32) is summarized in Table 9.

Table 9: Estimated parameters by radio luminosity

Name	L_{151}	$\log P_{\rm jet}$
	[10^{25}erg s^{-1}]	[erg s^{-1}]
IC 1531	0.49	43.2
NGC 315	0.22	42.89
NGC 1218	8.01	44.24
B3 0309+411B	19.67	44.57
IC 310	0.08	42.53
3C 111	25.93	44.68
3C 120	0.41	43.13
Pictor A	10.56	44.34
PKS 0521-36	13.92	44.44
PKS 0625-35	4.51	44.02
NGC 2484	6.66	44.17
3C 207	3116.89	46.46
B3 1009+427	21.56	44.61
B2 1113+29	5.94	44.13
3C2 64	3.83	43.96
3C 309.1	819.82	45.96
PKS 1514+00	2.98	43.87
NGC 6251	0.62	43.29
NGC 6328	0.16	42.77
3C 380	18781.09	47.13
PKS 2153-69	33.4	44.77
PKS 2331-240	2.53	43.81

I also calculated this jet power for the NVSS-SDSS sample which is a matched sample between the Sloan Digital Sky Survey (SDSS) DR7 Quasar catalog and the NARO Very Long Array Sky Servey (NVSS) catalog, following Inoue et al. (2017). The SDSS DR7 Quasar catalog is a catalog of 105,783 objects selected from the DR7 catalog (Schneider et al. (2010)), with detailed spectral properties provided by Shen et al. (2011). The NVSS catalog also covers the north sky with -40 degree declination at 1.4 GHz and has over 1.8 million objects in the entire survey. As with Inoue et al. (2017), this study used the same 30 arcsec radius‘ when SDSS DR7 was matched to the FIRST catalog to match the NVSS catalog and the SDSS DR7Quasar catalog and matched the closest objects within this radius. As a result, the total number of NVSS-SDSS samples was 24,053 objects. I note that in the SDSS DR7 Quasar catalog, the official notes about the possibility that targets other than Quasar have been selected [5]. The NVSS-SDSS sample was also applied with $R \equiv L_{\rm 5GHz}/L_{\rm B-band} \geq 10$ to limit the Radio-Loud AGNs (RL-Quasars). To calculate jet power and radio loudness, I assume a radio spectral index $\alpha = 0.8$ and the NVSS 1.4 GHz flux was converted to 151 MHz flux, and also, I assume an optical spectral index $\alpha = 0.5$ to convert SDSS optical flux to B-band flux.

6.2 Disk luminosity of RGs

The disk luminosity of my sample RGs should be estimated in MCMC method by adding disk/corona model to the SED model. However, for most sample RGs, it is found that it is difficult to estimate the jet model on multi-wavelength SED due to the lack of data for some frequencies, especially optical to UV data. Therefore, I decided not to use the disk/corona model as the SED fitting model in this study, and the disk luminosity is determined as the upper limit based on the X-ray emission characteristics discussed in Chapter 5. If the RG sample is a jet-dominant RG and an intermediate RG with more jet-like characteristics, it is considered that the disk is formed like ADAF and it appears a peak luminosity around optical to UV. In my sample RGs, optical data is well explained by the

[5] https://classic.sdss.org/dr7/products/value_added/qsocat_dr7.php

Swire galaxy template, therefore I defined UV luminosity as the upper limit disk luminosity. On the other hand, for disk/corona-dominant RGs and intermediate RGs with more disk/corona characteristics, I defined X-ray luminosity as the upper limit of disk luminosity. I summarize the estimated disk luminosity $L_{\rm disk}$ in Table 10.

For Blazers, Ghisellini et al. (2014) estimates the disk luminosity using the BLR luminosity, $L_{\rm BLR} = \phi L_{\rm disk}$ with $\phi \sim 0.1$ (Calderone et al. (2013)). For the NVSS-SDSS samples, the bolometric luminosity in the SDSS catalog was approximated as bolometric disk luminosity (Inoue et al. (2017)). This bolometric luminosity includes dust emission (infrared), accretion disk(optical), and disk/corona (X-ray) as disk luminosity.

Table 10: Jet power estimated by multiwavelength SED

Name	Template type[a]	logP_B	log$P_{\rm e}$	log$P_{\rm p}$	log$P_{\rm jet}$	log$L_{\rm disk}$
NGC 315	Ell2	44.87	43.88	44.86	45.19	42.82
NGC 5128	Sey2	44.36	44.8	45.47	45.58	43.42
3C 111	–	46.43	45.0	46.7	46.89	45.58
3C 120	–	46.65	44.73	46.26	46.8	45.27
3C 207	Ell2	40.75	46.43	47.96	47.98	46.59
3C 309.1	Ell2	40.75	46.55	48.22	48.23	46.99
3C 380	Ell2	30.14	53.47	55.41	55.41	47.21
B3 0309+411B	–	46.75	44.84	46.54	46.96	45.72
Pictor A	Ell2	43.09	45.53	47.14	47.15	44.69
PKS 0521-36	–	45.81	44.95	46.48	46.57	45.39
PKS 2331-240	–	44.56	45.29	46.63	46.65	45.0
PKS 0625-35	Ell2	41.72	43.59	44.91	44.93	46.5
NGC 6328	Ell2	45.7	43.6	45.26	45.83	43.88
B2 1113+29	Ell2	40.1	45.35	46.95	46.96	42.58
IC 1531	Ell2	43.14	45.05	46.91	46.92	42.24
NGC 1218	S0	44.25	45.46	47.39	47.39	42.42
3C 264	Ell2	45.01	44.35	46.13	46.17	41.91
B3 1009+427	–	40.24	43.9	44.81	44.86	44.58
NGC 2484	S0	42.61	45.6	47.54	47.54	42.33
NGC 6251	S0	44.8	44.64	45.62	45.72	46.17
PKS 1514+00	Ell2	47.05	44.0	45.6	47.06	42.69

[a] [a] This type means the host galaxy type and is used for Swire template. Ell2 means the 2 Gyr elliptical galaxy, Sey2 means type 2 Seyfert galaxy, and S0 means lenticular galaxy. I refer to morphology type in NASA/IPAC and decide the type of Swire template for each object, and I use Ell2 if there is no morphology classification in NASA/IPAC.

6.3 Results

I summarize the results of the parameters of sample RGs by SED model fitting using the MCMC mechanism in Table 11. Table 10 also summarizes jet power and its components calculated using these parameters.

Table 11: Estimated parameters by MCMC method

Name	log$B$	log$T$	logδ	logK_e	logγ_{break}	$P0$	$P1$	prior[a]
NGC315	0.727±0.00528	5.0	0.304±0.000643	46.605±0.0108	3.108±0.000990	1.334±0.00758	4.301±0.00186	
PKS0625-35	-1.981±0.0480	5.0	1.451±0.00506	43.764±0.00683	4.607±0.00525	2.002±0.000407	3.788±0.000255	
NGC6328	1.254±0.00342	5.0	0.187±0.000567	44.619±0.0752	3.487±0.0128	2.238±0.00101	5.798±0.160	
B21113+29	-2.521±0.427	5.0	1.179±0.0361	46.175±0.621	4.019±0.0688	2.208±0.0119	4.087±0.103	P1
NGC5128	0.766±0.000131	5.0	0.0	48.857±0.000895	2.51±8.39e-05	-3.249±0.252	4.05±3.36e-05	P1
IC1531	0.167±0.00472	5.0	0.0	39.872±0.228	5.473±0.0333	2.66±0.000287	4.131±0.181	P1
NGC1218	0.724±0.000210	5.0	0.0	40.818±0.0371	5.0±0.00360	2.869±8.25e-05	12.107±3.79	P1
3C264	1.102±0.00258	5.0	0.0	45.576±0.0881	3.184±0.00913	2.452±0.000385	3.13±0.00144	P1
B31009+427	-1.159±0.00260	5.0	0.0	42.1±0.0451	4.961±0.00761	1.799±3.40e-05	4.681±0.244	
3C111	1.822±0.000123	5.0	0.0	46.897±0.00398	3.021±0.000774	2.238±0.000110	4.348±0.00688	
3C120	1.927±3.298e-05	5.0	0.0	47.841±0.000130	2.636±3.69e-05	1.822±0.000108	3.986±0.000326	
NGC2484	-0.463±0.00915	5.0	0.371±0.000973	39.991±0.0234	5.421±0.00287	2.903±0.000127	11.996±3.85	P1
NGC6251	0.996±0.000555	5.0	0.0	48.022±0.00839	2.652±0.000997	0.951±0.0420	3.405±0.000635	
PKS1514+00	2.133±0.000545	5.0	0.0	47.221±0.00656	2.548±0.00104	1.93±0.000804	3.737±0.00148	
3C207	-2.295±0.0128	5.0	1.483±0.00102	47.941±0.0191	3.842±0.00331	2.10±0.00119	5.438±0.116	
3C309.1	-2.435±0.00851	5.0	1.675±0.000640	48.069±0.00826	3.769±0.00130	2.277±0.000164	4.657±0.0116	
3C380	-6.117±0.621	5.0	0.0	44.647±0.708	6.336±0.139	2.898±7.03e-05	2.013±0.00880	
B30309+411B	1.939±0.00659	5.0	0.077±0.000474	47.655±0.0106	2.677±0.00184	2.158±0.00174	3.825±0.00834	
PictorA	-0.47±0.0201	5.0	0.614±0.00160	46.983±0.00313	3.525±0.00334	2.17±9.90e-05	5.575±0.0731	
4C+40.01	-1.143±0.000409	5.0	0.0	47.51±0.00223	3.619±0.000500	2.014±0.000257	4.876±0.00952	
PKS0521-36	1.279±0.000754	5.0	0.235±5.07e-05	47.716±0.000277	2.861±0.000174	1.936±8.60e-05	3.738±0.000376	
PKS2331-240	0.887±0.000147	5.0	0.0	46.817±0.00115	3.406±0.000297	1.809±0.000141	7.566±0.126	

This table shows the result of the estimation values of multi-wavelength SED fitting using the MCMC method. I fixed some parameters depending on the multi-wavelength SED of each object, and then I fixed logT = 5.0 and logδ = 0.0.

[a] This column shows the prior distribution used in the MCMC method. I only used the prior distribution of P1, and I marked P1 for these objects.

Figure 22 shows the relationship between jet power and disk luminosity estimated from multi-wavelength SEDs. The NVSS-SDSS sample is not estimated from SEDs, thus only RG and Blazar are shown in this plot. Figure 22 shows that the RG sample has a wider distribution than Blazars. Here, I apply the X-ray origin type which I discussed in Chapter 5. Then, the disk/corona-dominant RG shows a distribution quite close to Ghisellini's Blazar sample. This plot exclude one object (3C 380) with high $L_{\rm disk}$ and $P_{\rm jet}$. I consider this object could not estimate the correct value since the $\gamma_{\rm break}$ estimated in MCMC method is quite high and thus the P_e and P_p values become higher compared with other RGs.

Also, Figure 6.3 shows the histograms of each power that composes the $P_{\rm B}$, $P_{\rm e}$, $P_{\rm p}$, and $P_{\rm jet}$ with the powers estimated in Ghisellini et al. (2014). From those histograms, I can see that most of the RGs show powers comparable to Blazar in each power. These values are summarized in Table 10.

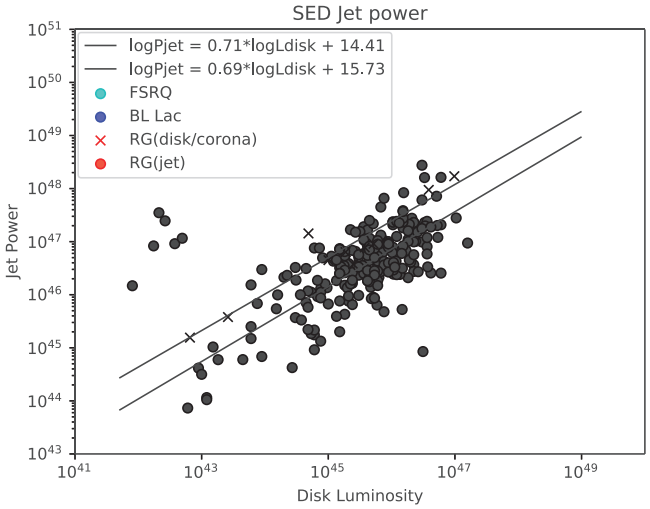

Figure 22: The relation between jet power estimated from SED and disk luminosity: The figure shows jet power calculated using parameters estimated from SED. Cyan and blue mean FSRQ and BL lac, respectively. Red means RG and "x" data is disk/corona-dominant RG and "+" data is jet-dominant RG. The line with dots and dashes is the regression line for disk/corona-dominant RG, showing $\log P_{\rm jet} = 0.69\ L_{\rm disk} + 15.73$. On the other hand, the solid line for Blazar shows a regression line with $\log P_{\rm jet} = 0.71\ L_{\rm disk} + 14.41$. Note that $L_{\rm disk}$ in RG is the upper limit value.

In this study, I use 2 ways of calculating jet power, and thus I need to confirm the difference in their jet power. Figure 6.4 shows the relationship between the jet powers in two ways. Figure 24 (left) shows the result of Ghisellini's Blazar sample, and these jet powers have almost the same values. On the other hand, For RGs in Figure 24 (right), these jet powers show nest correlation same as Blazar, but the jet power by SED shows 2-3 orders of magnitude higher than the power by radio luminosity. This plot also does not have 3C 380, and the left and right plots have the same scale axis.

Figure 25 shows the relation between disk luminosity and jet power which is estimated from radio luminosity by Blazer, RG, and NVSS-SDSS sample. NVSS-SDSS sample shows the regression line $\log P_{\rm jet} = 0.84\ \log L_{\rm disk} + 6.16$, and this relation is not in range of error of the regression line $\log P_{\rm jet} = 0.96(\pm 0.012)\ \log L_{\rm disk} + 0.79 \pm 0.55$ (Inoue et al. (2017)) but found quite close relation. RG is distributed over the entire NVSS-SDSS sample, whereas Blazar is consistent only with the upper part of the NVSS-SDSS. For disk/corona-dominant RGs, the regression line shows the middle of the regression line of Blazar and NVSS-SDSS samples. A fraction of NVSS-SDSS sample shows Blazar, and almost all of NVSS-SDSS sample shows RL-Quasar. Therefore, it is possible that NVSS-SDSS objects showing high $P_{\rm jet}/L_{\rm disk}$ are also classified as Blazar class.

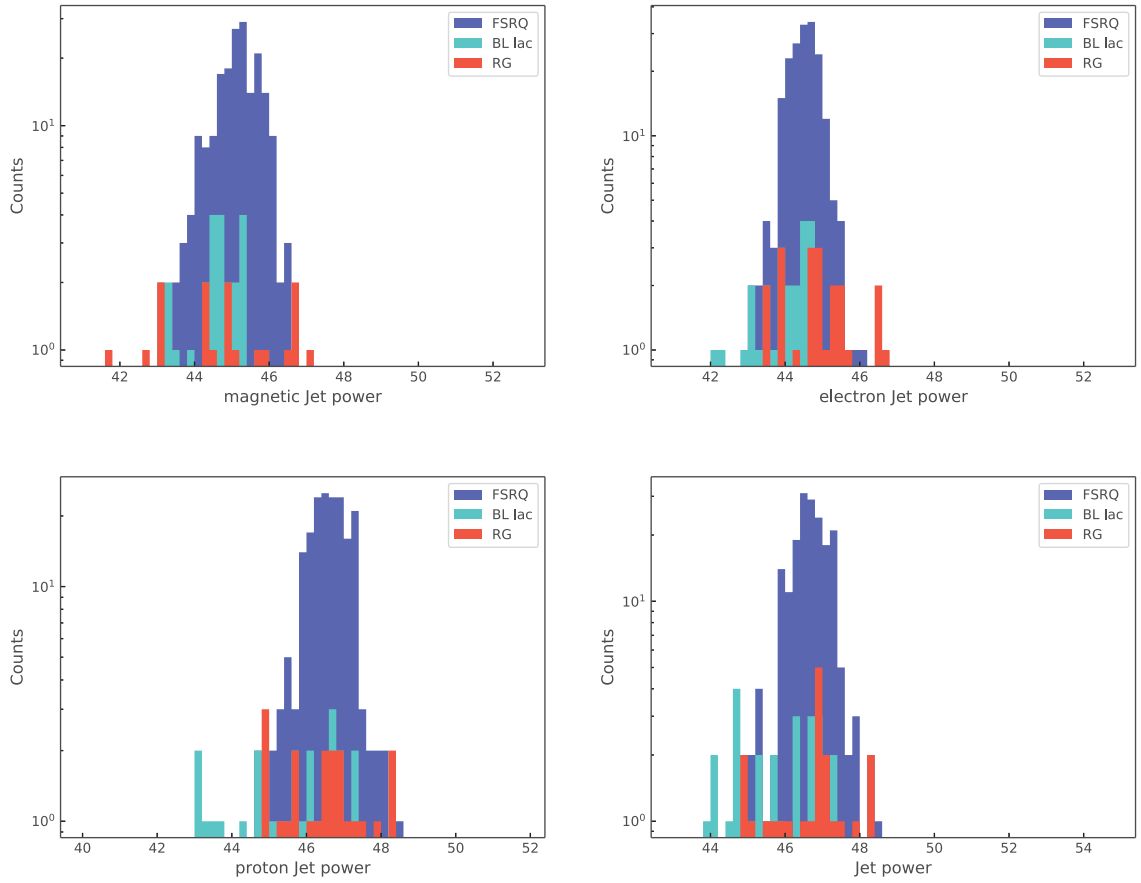

Figure 23: Jet power of magnetic field: The upper left is the jet power by magnetic field, the upper right is the jet power by electrons, the lower left is the jet power by protons, and the lower right is the total jet power. Blue is the Blazar of Ghisellini 14 and red is the RG sample of this study sample. 3C 380 is not included in the histogram range because of its extremely large value.

6.4 Discussion

In Figure 22, disk/corona-dominant RGs show a quite close relation with Blazar. The disk luminosity of these objects is considered that the origin of X-ray radiation is disk/corona and calculated using X-ray luminosity. Therefore, when the disk luminosity is properly estimated, the RG is found to be similar to Blazar which is observed jet dominantly.

On the other hand, for jet-dominant RG, I estimate the upper limit of disk luminosity using UV luminosity. This is because it is considered jet-dominant RG is formed like ADAF disk and optical and X-ray are dominated by host galaxy and jet radiation, respectively. For Ghisellini's Blazar sample, samples are observed with broad emission lines even if a class is BL lac. Thus, they would have an efficient accretion disk like a standard disk. Therefore, I consider that it is not appropriate to treat jet-dominant RGs with this Blazar sample and disk/corona-dominant RGs. In addition, objects are obviously grouped on the left side in Figure 22 and out of Blazar jet-disk relation. These objects show the same trend in Figure 6.4 (right), and thus the estimation of jet power from SED model fitting is correct. However, these jet-dominant RGs, which are NGC 1218, NGC 2484, 3C 264, IC 1531, B2 1113+29, have in common that they used prior distribution on P1, except for PKS 1514+00. In addition, their synchrotron peak is flat and I consider that this is because the SSC peak is flat. These things are caused by a flat gamma-ray

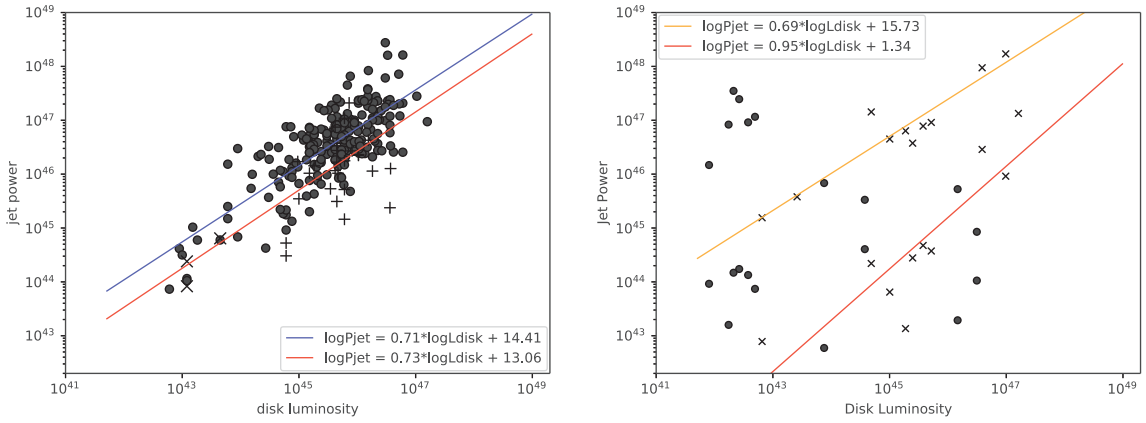

Figure 24: The relation between jet power by SED and jet power by radio luminosity in Blazars and RGs:
(left)The left figure is a Blazar plot. Jet power by SED is represented by FSRQ in cyan and BL lac in blue. Jet power from radio luminosity is represented by "+" for FSRQ and "x" for BL lac. Jet power calculated from SED shows a regression line of log $P_{\rm jet}$ = 0.71 log$L_{\rm disk}$ + 14.41 (blue line), while jet power calculated from radio luminosity shows a regression line of log$P_{\rm jet}$ = 0.73 log $L_{\rm disk}$ + 13.06 (red line).
(right)The right figure shows a plot of RG which has the same scale as Blazar plot (left), with the jet power from radio luminosity in red and that from SED in yellow, and the jet power of disk/corona-dominant RGs calculated from SED shows a regression line of log$P_{\rm jet}$ = 0.69 log$L_{\rm disk}$ + 15.73 (yellow line), while the jet power of disk/corona-dominant RG calculated from radio luminosity shows a regression line of log$P_{\rm jet}$= 0.95log$L_{\rm disk}$ + 1.34 (red line).

spectrum and a lack of data between X-ray to gamma-ray. I show a part of their result in Figure 6.4. Therefore, it is possible that their upper limit disk luminosity is underestimated and they show a closer relation to Blazar and disk/corona-dominant RGs in Figure 22. Therefore, for Blazar and disk/corona-dominant RGs, it is found that RGs and Blazars show $P_{\rm jet} \sim 10^2 L_{\rm disk}$ in Figure 22.

However, in Figure 6.4, the jet power calculated by radio luminosity was found to be comparable for Blazar, but about 2-3 orders of magnitude smaller for radio galaxies. In addition, Figure 25 showed the relation between jet power estimated by radio luminosity and disk luminosity using sample RGs, Blazars, and NVSS-SDSS sample (RL-Quasars). In this plot, the jet power of NVSS-SDSS sample showed a wider distribution than other objects, and a regression line of NVSS-SDSS sample showed the lowest jet power for disk luminosity. The plot also shows that Blazar, especially FSRQ, is consistent with the upper part of the NVSS-SDSS sample, and disk/corona-dominant RG is distributed between the regression lines of Blazars and NVSS-SDSS. As mentioned in the previous section, the upper part of NVSS-SDSS sample could be classified as Blazar. Here I give information on gamma-ray, which is considered to be a good indicator of jet radiation. Thus, I matched Ghisellini sample and the NVSS-SDSS sample to the Fermi 4FGL catalog and gave gamma-ray flux data. The closest object was matched to the Ghisellini sample within a 1 arcmin radius for matches and a 30 arcsec radius for matches to the NVSS-SDSS sample. Almost all of NVSS-SDSS samples were not observed by Fermi, and gamma-ray flux for them was given at their respective coordinates from the detective threshold map of the 4FGL-DR2 catalog. This map consists of 960 pixels of Galactic longitude and 481 pixels of Galactic latitude, and each unit has a gamma-ray flux value. This gamma-ray flux is estimated with the assumption that spectral shape is power-law for detective threshold map and power-law index is fixed 2.2, thus gamma-ray flux estimated used this map can have higher values than the value of the objects observed by Fermi.

Figure 6.4 (left) highlights NVSS-SDSS sample listed in the 4FGL catalog, and Figure 6.4 (right) shows gamma-ray flux versus 1.4 GHz radio flux. In the following, I refer NVSS-SDSS sample listed in the 4FGL catalog as the 4FGL NVSS-SDSS sample. Note that the gamma-ray flux estimated from the detective threshold is not a definite value but a guide, since it can vary. The 4FGL NVSS-SDSS consists of 236 objects, of which 136 (fsrq:129, FSRQ:7)

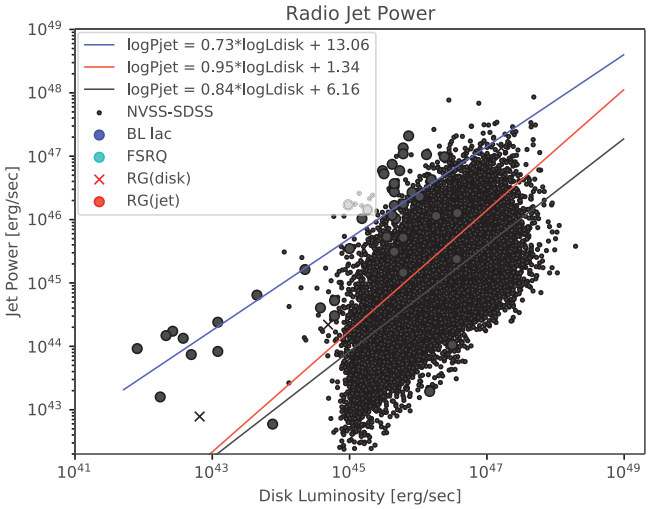

Figure 25: The figure plots the RGs, Blazar, and NVSS-SDSS samples using jet power calculated by radio luminosity. The black line in the figure is the regression line for the NVSS-SDSS sample created in this study, showing $\log P_{\rm jet} = 0.84\ \log L_{\rm disk} + 6.16$. Blue and Red lines show the regression lines of Blazars and RGs, respectively. Blazars show $\log P_{\rm jet} = 0.73\ \log L_{\rm disk} + 13.06$, RGs show $\log P_{\rm jet} = 0.95\ \log L_{\rm disk} + 1.34$

were FSRQ and 43 (bll:42, BLL:1) were BL lac. The others were NLSY1:2, bcu:25, css:1, nlsy1:3, rdg:1, sbg:2, and the rest were considered unclassified. Thus, more than half of the 4FGL NVSS-SDSS sample is classified as Blazar at 4FGL. In Figure 6.4 (left), it is found that the FSRQ of the 4FGL NVSS-SDSS sample distributes between the regression line of Ghisellini blazar sample and disk/corona-dominant RG, and upper part of them shows a very close distribution to Ghisellini blazar sample. The Ghisellini sample selection is based on the requirement that the object is observed by Fermi and optical emission lines from the BLR are observed. Therefore, BL lac objects of Ghisellini sample are expected to be close to the FSRQ objects, and I consider that the upper part of the FSRQ of the 4FGL NVSS-SDSS sample matches with the FSRQ of Ghisellini sample. However, for the BL lac objects in the 4FGL NVSS-SDSS sample, the jet power relative to the disk luminosity is too low to be considered equivalent to the Ghisellini FSRQ sample. I consider that the regression line of RGs can explain the highlighted object, except for the upper part of FSRQ. For the NVSS-SDSS samples which are not detected by Fermi, it is found that they have a trend that most of them have lower radio flux values in Figure 6.4 (right). In addition, the highlighted objects in Figure 6.4 (left) show relatively high jet power relative to the disk luminosity, while the NVSS-SDSS sample, which is not detected in gamma-rays, seems to show relatively low jet power relative to the disk luminosity, suggesting that these objects are the original RL-Quasar. I consider that the variation in jet power among the objects is due to the observed radio luminosity being affected by the beaming effect. The RGs used in this study are gamma-ray-detected objects by Fermi. The RGs detected in Fermi also show relatively small inclination angles (Pushkarev et al. (2017), Kayanoki & Fukazawa (2022)), so the beaming effect is expected to work strongly compared to the undetected RGs and the NVSS-SDSS sample. Blazar is also known in lots of papers to have higher Doppler and Lorentz factors for FSRQ than for BL lac (Hovatta et al. (2009), Liodakis et al. (2017)). Thus, in Figure 6.4 (right) the Blazar would have the highest jet power relative to disk luminosity, the RG in this study and the BL lac would have the next highest relationship, and the RL-Quasar would have the lowest relationship. Therefore, the calculation of jet power by radio luminosity (Eq. 32) is not considered accurate.

Moreover, considering the formula for radio luminosity (Eq. 32), the only parameters used in this formula are the correction parameter f and the radio luminosity at one wavelength. The correction parameter f has multiple corrections. In addition, it is $1 \leqslant f \lesssim 20$ and can only take a very narrow range of values. Therefore, it is possible that the estimation by radio luminosity may not properly estimate the jet power. In contrast, the estimation by multiwavelength SED is more reliable in estimating values because it uses data from all wavelengths and estimates

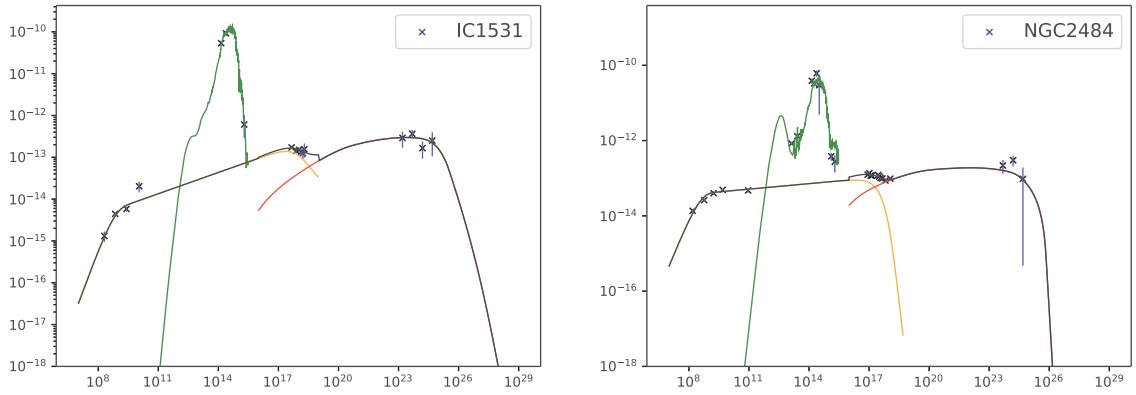

Figure 26: These plots show the result of the SED model fitting of IC 1531 and NGC 2484. These plots are one of the jet-dominant RG on the left part in Figure 22. The blue cross shows spectral data. The yellow line shows the synchrotron model, the red line shows the SSC model and the black line shows the total model of the synchrotron and SSC model. The green line also shows the Swire template. They have flat gamma-ray and prior distribution of P1 in common.

jet model (Synchrotron + SSC model) parameters to calculate jet power. In addition, the Ghisellini sample consists of only objects for which sufficient multi-wavelength data were available. For RG in this study, more than half of the objects showed distributions similar to the Ghisellini sample. However, sufficient frequency data were not available for a large number of objects, and it was necessary to fix some parameters for all of them. Thus, I note that the original emission may not have been reproduced by the jet model.

From the above, it was found that the jet power estimated by SED is appropriate for investigating the relationship between disk luminosity and jet power. Here, I express disk luminosity and jet power using the energy of accretion matter $\dot{m}c^2$.

$$L_{\rm disk} = f\dot{m}c^2 \quad (33)$$
$$P_{\rm jet} = 100f\dot{m}c^2 \quad (34)$$

It is known that BH of RG and Blazar have $10^{9-10}M_{\odot}$ and then the Eddington luminosity shows $L_{Edd} \approx 2 \times 10^{47-48}$[erg/sec]. In the Figure 22, the objects located upper right showing $L_{\rm disk} = 10^{46-47}$ have a 10 % of this L_{Edd} and thus it is considered that the accretion disk of these objects has standard disk. If objects show standard disk, the parameter f shows $f = 0.1$. Therefore, jet power is 10 times higher than the energy of accretion matter. This is considered to be due to the extraction of rotational energy by the Blandford-Znajek(BZ) mechanism as in the case of the Blazar (Ghisellini et al. (2014)).

6.5 Conclusion

In this chapter, I investigate the relationship between jet power and disk luminosity using two methods. First, for the jet power by multiwavelength SED model fitting, I compared Ghisellini's Blazar sample with my sample RGs and found that disk/corona-dominant RGs show a relationship similar to the distribution of the Blazar sample. It is considered that Ghisellini's Blazar samples show efficient accretion disk and thus it is reasonable disk/corona-dominant RGs are distributed along this Blazar sample, and it is considered that this disk luminosity is estimated